Trans-Lesion Synthesis and Mismatch Repair Pathway Crosstalk Defines Chemoresistance and Hypermutation Mechanisms in Glioblastoma

Xing Cheng

   Chongqing University Cancer Hospital & Chongqing Cancer Institute & Chongqing Cancer Hospital

Jing An

   Heilongjiang Academy of Medical Sciences, Harbin Medical University

Jitong Lou

   University of North Carolina at Chapel Hill   https://orcid.org/0000-0002-1049-0416

Qisheng Gu

   Institut Pasteur of Shanghai, Chinese Academy of Sciences

Weimin Ding

   Southern Medical University

Gaith Droby

   University of North Carolina at Chapel Hill   https://orcid.org/0000-0003-0116-0340

Yilin Wang

   University of North Carolina at Chapel Hill   https://orcid.org/0000-0002-1255-767X

Chenghao Wang

   University of North Carolina

Yanzhe Gao

   University of North Carolina at Chapel Hill

Abigail Shelton

   University of North Carolina

Andrew Satterlee

   University of North Carolina

Breanna Mann

   University of North Carolina   https://orcid.org/0000-0002-6486-3230

Yun-Chung Hsiao

   UNC-Chapel Hill   https://orcid.org/0000-0003-1189-6511

Chih-Wei Liu

   University of North Carolina at Chapel Hill   https://orcid.org/0000-0002-0823-0252

Kun Lu

   University of North Carolina at Chapel Hill

Shawn Hingtgen

University of North Carolina at Chapel Hill   https://orcid.org/0000-0003-4355-2377

Jiguang Wang

The Hong Kong University of Science and Technology   https://orcid.org/0000-0002-6923-4097

Zhaoliang Liu

Heilongjiang Academy of Medical Sciences, Harbin Medical University   https://orcid.org/0000-0002-2074-1522

C Miller

University of Alabama at Birmingham Heersink School of Medicine   https://orcid.org/0000-0002-0096-8762

Di Wu

University of North Carolina at Chapel Hill   https://orcid.org/0000-0001-8331-2357

Cyrus Vaziri

UNC

Yang Yang (✉ yangyang@email.unc.edu)

University of North Carolina at Chapel Hill   https://orcid.org/0000-0002-5936-4090

Article

Keywords:

Additional Declarations: Yes there is potential Competing Interest. B.M., S.H., and A.S. have submitted a provisional patent application based on the OBSC work in this manuscript

---

Trans-Lesion Synthesis and Mismatch Repair Pathway Crosstalk Defines Chemoresistance and Hypermutation Mechanisms in Glioblastoma

Xing Cheng[1,2,†], Jing An[1,3,†], Jitong Lou[4,†], Qisheng Gu[5,6†], Weimin Ding[7,8], Gaith Droby[1,9], Yilin Wang[1], Chenghao Wang[4], Yanzhe Gao[1], Abigail Shelton[1], Andrew Benson Satterlee[10], Breanna Elizabeth Mann[10], Yun-Chung Hsiao[11], Chih-Wei Liu[11], Kun Liu[11], Shawn Hingtgen[10], Jiguang Wang[12,13], Zhaoliang Liu[3], Ryan Miller[1,14], Di Wu[4,7,15], Cyrus Vaziri[1,7*,#] and Yang Yang[1,7*]

[1] Department of Pathology and Laboratory Medicine, University of North Carolina, Chapel Hill, NC 27599, USA
[2] Department of Neuro-Oncology, Chongqing University Cancer Hospital & Chongqing Cancer Institute & Chongqing Cancer Hospital, Chongqing, China
[3] Institute of Cancer Prevention and Treatment, Heilongjiang Academy of Medical Sciences, Harbin Medical University, Harbin, China
[4] Department of Biostatistics, University of North Carolina, Chapel Hill, NC 27599, USA
[5] Unit of Immunity and Pediatric Infectious Diseases, Institute Pasteur of Shanghai, Chinese Academy of Sciences, Shanghai, China.
[6] Department of Immunology, Université Paris Cité, Paris, France
[7] Lineberger Comprehensive Cancer Center, University of North Carolina, Chapel Hill, NC 27599, USA
[8] Oncology Center, Zhujiang Hospital, Southern Medical University, Guangzhou, China
[9] Curriculum in Genetics and Molecular Biology, University of North Carolina, Chapel Hill, NC 27599
[10] Eshelman School of Pharmacy, Division of Pharmacoengineering and Molecular Pharmaceutics, University of North Carolina, Chapel Hill, NC 27599
[11] Department of Environmental Sciences and Engineering, University of North Carolina at Chapel Hill, Chapel Hill, NC, 27599, USA
[12] Division of Life Science, Department of Chemical and Biological Engineering, State Key Laboratory of Molecular Neuroscience, The Hong Kong University of Science and Technology, Hong Kong SAR, China
[13] Hong Kong Center for Neurodegenerative Diseases, InnoHK, Hong Kong SAR, China.
[14] Department of Pathology, Division of Neuropathology, Heersink School of Medicine, University of Alabama at Birmingham, Birmingham, Alabama, USA
[15] Division of Oral and Craniofacial Health Science, Adams School of Dentistry, University of North Carolina at Chapel Hill, Chapel Hill, NC, USA

*Co-corresponding authors: yangyang@email.unc.edu; cyrus_vaziri@med.unc.edu
[#] To whom reagent requests should be sent: cyrus_vaziri@med.unc.edu
[†] These authors contributed equally to this work as the first authors

41 **ABSTRACT**
42
43 Almost all Glioblastoma (GBM) are either intrinsically resistant to the chemotherapeutical drug
44 temozolomide (TMZ) or acquire therapy-induced mutations that cause chemoresistance and
45 recurrence. The genome maintenance mechanisms responsible for GBM chemoresistance and
46 hypermutation are unknown. We show that the E3 ubiquitin ligase RAD18 (a proximal regulator of TLS)
47 is activated in a Mismatch repair (MMR)-dependent manner in TMZ-treated GBM cells, promoting post-
48 replicative gap-filling and survival. An unbiased CRISPR screen provides a new aerial map of RAD18-
49 interacting DNA damage response (DDR) pathways deployed by GBM to tolerate TMZ genotoxicity.
50 Analysis of mutation signatures from TMZ-treated GBM reveals a role for RAD18 in error-free bypass of
51 O^6mG (the most toxic TMZ-induced lesion), and error-prone bypass of other TMZ-induced lesions. Our
52 analyses of recurrent GBM patient samples establishes a correlation between low RAD18 expression
53 and hypermutation. Taken together we define novel molecular underpinnings for the hallmark
54 tumorigenic phenotypes of TMZ-treated GBM.
55

INTRODUCTION

Glioblastoma (GBM) patients have a dismal prognosis with a median survival of only nine months without treatment, which modestly improves to 15–16 months following standard-of-care surgery and adjuvant chemoradiation [1]. Temozolomide (TMZ) is a DNA methylating chemotherapeutic agent used in the treatment of brain cancers and is the only FDA-approved first-line chemotherapeutic drug for glioblastoma (GBM) [2]. TMZ induces N^7-methyl guanine (N^7mG), 3-methyl adenine (N^3mA) and O^6-methyl guanine (O^6mG) lesions, each contributing approximately 70%, 25% and 5% of the total TMZ-induced DNA damage respectively [3]. In most cells N^7mG and N^3mA lesions generate apurinic sites that are ultimately repaired by the Base Excision Repair (BER) pathway [4]. Although O^6mG comprise < 5% of all TMZ-induced lesions, this species is considered to mediate the toxic and anti-neoplastic effects of TMZ [5]. Cells expressing the suicide enzyme O^6-methylguanine-DNA methyltransferase (MGMT) directly remove O^6mG adducts and are refractory to TMZ-induced toxicity [6,7]. O^6mG does not directly interfere with or perturb DNA synthesis. Instead, it is thought that O^6mG adducts mis-pair with thymine during the first round of DNA replication following alkylation damage [8]. However, lethal DNA damage and cytotoxicity arises in a second cell cycle due to the action of MMR machinery [9-12].

The MMR pathway detects O^6mG:T mis-matches and removes the mis-paired thymine residues [13,14]. However, the O^6mG lesion persists and MMR-mediated gap-filling reforms the O6mG:T mis-pair resulting in additional futile MMR cycles [15-19]. The precise mechanism by which MMR futile cycling leads to cytotoxicity has yet to be established. A widely-favored model posits that the long single-stranded DNA (ssDNA) gaps generated by futile MMR cycles interfere with DNA replication forks [20,21]. However, the specific DNA repair and DNA replication fork-protective mechanisms that allow GBM to tolerate TMZ-induced lesions remain poorly characterized. Therefore, defining the DNA damage response (DDR) effector pathways that respond to TMZ-induced DNA lesions may reveal new vulnerabilities and opportunities for GBM therapy.

All GBM eventually become TMZ-refractory and recur [22]. It is suggested that therapy-induced mutations account for the adaptations that allow GBM to resist TMZ. Hypermutation (i.e. a high mutation burden) is rare in newly-diagnosed gliomas, but has been described in recurrent tumors from TMZ-treated patients [23-25]. The extent to which TMZ-induced hypermutation causes GBM recurrence is still debated [25]. Nevertheless, it is clear that tumors from TMZ-treated GBM patients harbor a specific mutational signature (designated Single Base Substitution 11 or SBS 11) which is characterized by a preponderance of G:C>A:T transitions at non-CpG sites [26]. MMR pathway dysfunction and MGMT gene promoter methylation are associated with hypermutation [24,27-30]. However, the underlying mechanisms that mediate therapy-induced mutation signatures and lead to hypermutation only in a subset of recurrent GBM (rGBM) are not fully understood.

Here we sought to elucidate the DDR mechanisms that allow GBM to tolerate TMZ-induced genotoxicity and mediate therapy-induced mutagenesis. Trans-Lesion Synthesis (TLS) pathway is a DNA damage-tolerant and error-prone mode of DNA replication. TLS relies on specialized error-prone 'Y-family' DNA polymerases to replicate damaged templates and fill the post-replicative ssDNA gaps, including gaps arising due to spontaneous DNA replication defects in cancer cells [31-33]. Thus, TLS could provide a potential explanation for two major hallmarks of treatment-refractory GBM, namely DNA damage-tolerance and mutability.

Recruitment of the Y-family TLS polymerases to damaged DNA is facilitated by the E3 ubiquitin ligase RAD18 [34]. RAD18 is recruited to sites of DNA replication stalling or repair synthesis via direct interactions with Replication Protein A (RPA)-coated ssDNA [35,36]. RAD18 then mono-ubiquitinates the conserved residue K164 of PCNA molecules residing in the vicinity of damaged DNA. Interactions between Y-family polymerases and mono-ubiquitinated PCNA constitute a 'TLS polymerase switch' that

107 activates post-replicative repair synthesis [37]. Because RAD18 is a proximal master regulator of TLS
108 polymerases, we tested a role for RAD18 in the response to TMZ-induced genotoxicity. We show that
109 a RAD18-Polκ signaling axis is activated in an MMR-dependent manner in TMZ-treated GBM and
110 contributes to cell survival. Additionally, our unbiased genetic screens reveal the RAD18-interacting
111 DDR network that contributes to tolerance of TMZ-induced DNA damage. Finally, our analysis of
112 genomes from TMZ-treated GBM cells defines the contribution of RAD18 to TMZ-induced mutational
113 scars. Taken together, our work provides an unparalleled mechanistic view of how intersecting
114 genome maintenance pathways mediate ssDNA gap repair, confer survival and reshape the genome in
115 the important disease setting of GBM.

117 **RESULTS**

119 **TMZ activates the RAD18-mediated TLS pathway in astrocytes and GBM cell lines**

121 To determine whether the RAD18 pathway is activated in response to TMZ, we measured levels of
122 mono-ubiquitinated PCNA in TMZ-treated astrocyte and GBM lines. As shown in Fig. 1A-C, TMZ
123 induced a robust PCNA mono-ubiquitination response in HRAS-transformed normal human astrocytes
124 (NHARas) [38], and in the MGMT-deficient U87 and U373 GBM cell lines. TMZ treatment redistributed
125 RAD18 to RPA-containing nuclear puncta representing DNA repair foci (Fig. 1D). TMZ-induced PCNA
126 mono-ubiquitination was abrogated in *RAD18*^{-/-} U373 cells (Fig. 1C). In the absence of *RAD18*, TMZ-
127 treatment led to elevated expression of phospho-ATM and phospho-CHK1 (Fig. 1C), markers of DNA
128 DSB and ssDNA gaps respectively. Therefore, TMZ-induced DNA damage promotes RAD18-
129 dependent PCNA mono-ubiquitination and averts formation of persistent secondary DNA gaps and
130 breaks.

132 PCNA mono-ubiquitination levels peaked 24-48 h following TMZ treatment (Fig. 1C). The delayed
133 kinetics of PCNA-mono-ubiquitination suggest that TMZ-induced RAD18 activation requires a second
134 round of DNA synthesis. Indeed, the number of cells actively synthesizing DNA was not significantly
135 affected during the first 24 h of TMZ-treatment (Fig. 1E). However, 48 h post-TMZ treatment, we
136 observed accumulation of BrdU-positive cells with late-S/G2 DNA content (Fig. 1E). Supplementary
137 Fig. 1 shows that in nocodazole-synchronized cells PCNA mono-ubiquitination peaks in the second cell
138 cycle following TMZ treatment. Critically, nocodazole treatment to block passage into a second cell
139 cycle abrogated the TMZ-induced PCNA mono-ubiquitination.

141 In *RAD18*-deficient cells, DNA synthesis rates during late S-phase/G2 were reduced when compared
142 with *RAD18*^{+/+} U373 cells (Fig. 1E). These results suggest that RAD18 mediates post-replication repair
143 of TMZ-induced DNA damage. In contrast with U373 cells, TMZ treatment induced only a modest level
144 of PCNA mono-ubiquitination in LN18 cells which express MGMT and do not accumulate O^6mG (Fig.
145 1F). However, in LN18 cells co-treated with an MGMT inhibitor, O^6-benzylguanine (O^6bG), TMZ
146 induced robust PCNA mono-ubiquitination (Fig. 1F). RAD18-loss did not affect steady-state levels of
147 O^6mG (Fig. 1G). We conclude that TMZ-induced primary O^6mG lesions undergo processing during a
148 second replicative cycle, to generate secondary lesions that are repaired by the RAD18 pathway.

150 **RAD18 depletion sensitizes GBMs to TMZ**

152 TMZ treatment induced RAD18-dependent PCNA-mono-ubiquitination in both NHA and NHARas cell
153 lines (Fig. 2A). In clonogenic survival assays, RAD18-depletion led to increased TMZ-sensitivity in
154 NHARas cells but not in untransformed NHA (Fig. 2B). *RAD18*^{-/-} derivatives of U373 and U87 GBM cell
155 lines were also TMZ-sensitive when compared with isogenic *RAD18*^{+/+} parental cells (Figs. 2C-D). In
156 contrast with MGMT-deficient U373 and U87 cells, MGMT-expressing LN18 GBM cells were not
157 sensitized to TMZ by RAD18 ablation (Fig. 2E). However, LN18 cells treated with the MGMT inhibitor

158   O^6bG were TMZ-sensitive (Fig. 2E). *RAD18* knockout further sensitized O^6bG-treated cells to TMZ
159   when compared with parental (*RAD18^{+/+}*) LN18 cells. These results are consistent with Fig. 1F in which
160   O^6bG-treated *RAD18^{-/-}* LN18 cells expressed increased levels of DNA damage markers (pATM,
161   pRPA32 and γH2AX) when compared with parental LN18 cells. We conclude that RAD18 mediates
162   repair and tolerance of O^6mG lesions.
163
164   In MGMT-expressing GBM (which do not accumulate O^6mG), other TMZ-induced lesions N^3-methyl
165   adenine (N^3mA) and N^7-methyl guanine (N^7mG), can be repaired by BER [39]. We measured TMZ-
166   sensitivity of parental and *RAD18^{-/-}* LN18 cells in the presence and absence of methoxyamine (MeOX),
167   a BER inhibitor [40,41]. As shown in Fig. 2F, RAD18 ablation led to TMZ-sensitivity of LN18 cells only
168   when we inhibited BER. Therefore, BER and RAD18 are redundant pathways for repair of N^3mA and
169   N^7mG lesions in MGMT-expressing cells. As shown in Fig. 2G, RAD18-ablation and BER inhibition had
170   synergistic effects on TMZ-sensitivity in U373 cells. Therefore, in MGMT-deficient cells (in which the
171   main cytotoxic lesion is O^6mG), BER and RAD18 participate in distinct pathways for tolerance of TMZ-
172   induced lesions. Taken together, the results of Fig. 2G identify interactions between RAD18, BER and
173   MGMT-mediated DNA repair pathways, and reveal RAD18 as a new vulnerability of both MGMT-
174   deficient and MGMT-expressing GBM. To further validate RAD18 as a dependency of GBM, we
175   determined the TMZ-sensitivity of *RAD18^{+/+}* and *RAD18^{-/-}* GBM cells cultured in a newly-developed
176   organotype brain slice culture (OBSC) platform [42]. As shown in Fig. 2H-I, *RAD18^{-/-}* U373 cells cultured
177   on brain slices were highly sensitive to TMZ cytotoxicity when compared with *RAD18*-sufficient parental
178   cells. Taken together, the results of Fig. 2 identify a new role for RAD18 in tolerating TMZ-induced
179   cytotoxicity in GBM.
180
181   **TMZ-induced RAD18 pathway activation is MMR-dependent**
182
183   48 h after TMZ treatment, we observed reduced BrdU incorporation and an increase in the G2/M-
184   arrested populations of *RAD18^{-/-}* cells relative to *RAD18^{+/+}* control cultures (Figs. 1E and 3A). Flow
185   cytometric analysis of mitosin + phospho-histone H3 doubly-stained nuclei also indicated more robust
186   TMZ-induced G2 arrest in *RAD18^{-/-}* cells when compared with *RAD18^{+/+}* (Fig. 3B, Supplementary Fig.
187   2). After 48 h of TMZ treatment, RAD18-deficent cells in G2 contained approximately twice as many
188   phospho-RPA (ssDNA marker) and γH2AX (DSB marker) double-positive nuclei when compared with
189   *RAD18^{+/+}* cells (Fig. 3C). Interestingly, our analysis of scRNA gene expression data obtained from
190   fresh primary GBM tumors [43] revealed that *RAD18* expression was higher in S/G2 phase cells
191   compared with cells in G1 (Fig. 3D, Supplementary Fig. 3). This finding is further consistent with an
192   important role for RAD18 in preventing accumulation of post-replicative DNA damage. We conclude
193   that RAD18 prevents accumulation of TMZ-induced post-replicative single-stranded DNA gaps and
194   DSB, averting G2 arrest.
195
196   In TMZ-treated cells lacking MGMT, O^6mG-thymine mis-pairs are recognized by mismatch repair
197   (MMR) and subsequent futile cycles of DNA repair and thymine reinsertion generate DNA damage [8,44].
198   As shown in Fig. 3C, TMZ treatment did not increase the ssDNA and DSB double-positive population in
199   *MLH1^{-/-}* cells. RAD18-ablation led to persistence of DNA damage markers (pCHK1 and pCDC2) in
200   TMZ-treated MMR-sufficient, but not in MMR-deficient (*MLH1^{-/-}*) cells (Fig. 3E). MMR-sufficient cells
201   were sensitized to TMZ (as measured by clonogenic survival assays) upon RAD18-depletion (Fig. 3F).
202   However, isogenic cells lacking *MLH1* or *MSH2* were not TMZ-sensitive after RAD18 ablation (Fig. 3F).
203   TMZ induced robust PCNA ubiquitination in MMR+ cells but not in isogenic cells lacking *MLH1* or
204   *MSH2* (Figs. 3 E&G). Therefore, MMR-mediated processing of TMZ-induced lesions is required for
205   RAD18 pathway activation. In MGMT-expressing LN18 cells which do not accumulate O^6mG, RAD18-
206   ablation did not lead to persistent DDR signaling after TMZ treatment (Fig. 3H). It is known that
207   following mispair recognition, the nuclease EXO1 excises the daughter strand to expose ssDNA.
208   Ablating EXO1 (using siRNA) led to attenuation of PCNA mono-ubiquitination (Fig. 3I). Taken together,

209 the results of Fig. 3 suggest that TMZ-induced O^6mG lesions are processed by MMR to generate
210 ssDNA gaps that recruit RAD18 to promote PCNA mono-ubiquitination and DNA damage tolerance.
211
212 **Polκ mediates TMZ-tolerance**
213
214 To test whether Y-family DNA polymerases mediate TMZ-tolerance, we used siRNA to ablate *POLK*,
215 *POLH*, and *POLI* individually, or we used the pharmacological agent JH-RE-06[45] to inhibit REV1. As
216 shown in Fig. 4B, Polκ-depleted cells (but not cells deficient in Polη, Polι or REV1) were TMZ-sensitive,
217 suggesting a role for Polκ in repair of TMZ-induced DNA damage. Analysis of TCGA data revealed that
218 low-grade glioma patients with high-level expression of *RAD18* and *POLK* showed reduced survival
219 probability when compared with *RAD18*-low and *POLK*-low groups respectively (Supplementary Fig. 4).
220 In TMZ-treated cells a GFP-Polκ fusion protein formed nuclear foci in a *RAD18*- and *MLH1*-dependent
221 manner (Fig. 4C). We conclude that MMR-dependent processing of TMZ-induced O^6mG lesions
222 generates secondary DNA damage (likely ssDNA) that activates RAD18, promoting PCNA mono-
223 ubiquitination and Polκ-mediated repair synthesis.
224
225 *POLK^{-/-}* U373 cells generated by gene editing partially phenocopied the TMZ-sensitivity of *RAD18^{-/-}*
226 cells (Fig. 4D). TMZ-sensitivity of *POLK^{-/-}* cells was further exacerbated by RAD18-loss, indicating that
227 Polκ may also have RAD18-independent roles in TMZ-tolerance. Polη inserts C or T across O^6mG
228 lesions [46]. Therefore we tested a role for Polη as another effector of RAD18-dependent TMZ-tolerance.
229 YFP-Polη was redistributed to nuclear repair foci following TMZ-treatment in *RAD18^{+/+}* but not *RAD18^{-/-}*
230 U373 cells (Fig. 4E). Surprisingly, *POLH* knockdown using siRNA led to decreased TMZ-sensitivity in
231 both *RAD18^{+/+}* and *RAD18^{-/-}* U373 cells. However, *POLH* siRNA did not affect TMZ-sensitivity in *POLK^{-/-}*
232 cells (Fig. 4F). To elucidate the relationship between Polκ and Polη in the TMZ response, we
233 quantified GFP-Polκ foci in *POLH*-depleted cells. As shown in Fig. 4G, *POLH* knockdown led to an
234 increased percentage of cells with PCNA-colocalizing GFP-Polκ foci. We infer that Polη interferes with
235 Polκ PCNA-binding and reduces tolerance of TMZ-induced lesions.
236
237 **Defining an integrative network of the DNA damage response to TMZ**
238
239 To comprehensively define the genome maintenance network (including RAD18-interacting pathways)
240 that mediates tolerance of TMZ-induced DNA damage, we performed a CRISPR-based loss-of-function
241 screen. We transduced *RAD18^{+/+}* and *RAD18^{-/-}* U373 cells with a sgRNA library targeting 504 DNA
242 Damage Response (DDR) genes spanning every major DNA repair pathway (Supplementary Table 1).
243 Stably-infected cells were grown for 20 population doublings (PD) in the presence or absence of TMZ.
244 Finally we sequenced lentivirus integrated cassette DNA to quantify abundance of each sgRNA
245 sequence relative to all mapped reads for each experimental group (Fig. 5A, Supplementary Table 2).
246 Fig. 5B plots the normalized counts for all sgRNAs in U373 *RAD18^{+/+}* (blue) and *RAD18^{-/-}* (purple) cells
247 under different experimental conditions. *RAD18*-deficiency did not affect the distribution of control non-
248 targeting sgRNAs (NTsgRNA) after 20 PDs in the DMSO-treated cultures. However, we observed a
249 significant reduction in the NTsgRNA count in the *RAD18^{-/-}* line when compared to the RAD18^{+/+} cells
250 after 20 PDs in the presence of TMZ treatment. These results indicate that RAD18-loss compromises
251 cell viability under TMZ treatment conditions. Furthermore, we noticed a striking depletion of many
252 DDR-targeting sgRNAs in the TMZ-treated *RAD18^{-/-}* cells when compared with *RAD18^{+/+}*. This result
253 indicates a broad general dependency on multiple back-up DNA damage tolerance pathways when
254 RAD18 is absent. The volcano plots in Fig. 5C represent the sigma fold-change (sigmaFC) in Gene
255 Abundance Change Scores vs the statistical significance of depletion or enrichment (Supplementary
256 Table 3). As expected, sgRNAs targeting MMR genes (*MLH1*, *MSH6*, *PMS1*, *PMS2* and *MSH2*) were
257 highly enriched in TMZ-treated cells, regardless of *RAD18* genotype (Fig. 5C). This positive selection

258 for sgRNAs targeting MMR genes in TMZ-treated cells reflects the role of MMR in generating lethal
259 secondary DNA damage from primary TMZ-induced O^6mG lesions, and validates our screen.
260
261 To identify the most important mechanisms for TMZ-tolerance in $RAD18^{+/+}$ and $RAD18^{-/-}$ cells, we
262 grouped sgRNAs according to their corresponding DDR pathway(s) and compared relative dropout of
263 the different DDR pathway groups between experimental conditions. The heatmaps in Fig. 5D show
264 the relative dropout of sgRNAs targeting mediators of different branches of the DDR under our screen
265 conditions (Supplementary Tables 4&5). Interestingly, sgRNAs targeting components of the Fanconi
266 Anemia (FA), HR, and checkpoint signaling pathways were preferentially depleted in TMZ-treated cells
267 compared with DMSO-treated control cultures (Fig. 5D), likely indicating that DSB are the ultimate
268 lethal lesions induced by TMZ. Furthermore, FA, NHEJ, checkpoint signaling, and mitosis/spindle
269 assembly checkpoint pathways were preferentially depleted in $RAD18^{-/-}$ cells, indicating that cells rely
270 on these pathways to process DSB repair when RAD18 is missing (Fig. 5E). This result is consistent
271 with results of Fig. 1 showing a role for RAD18 in suppressing the formation of lethal DSB following
272 TMZ treatment. Fig. 5D&E also indicates minor backup roles for BER, NER, PARP, TS, and nucleotide
273 metabolism in TMZ-treated $RAD18^{-/-}$ cultures compared with TMZ-treated $RAD18^{+/+}$ cells.
274
275 Based on significance of drop-out of corresponding sgRNAs (Supplementary Fig. 5A), we selected
276 several DDR factors for independent validation of new roles in TMZ-tolerance. We used
277 pharmacological agents to inhibit CHK2 (PV1019) or DNA-PKs (NU7441) in $RAD18^{+/+}$ and $RAD18^{-/-}$
278 cells. The synergy distribution plots and inhibition scores in Fig. 5E and 5F show that both CHK2 and
279 DNA-PKs inhibitors synergize with low doses of TMZ to kill $RAD18^{-/-}$ cells. In $RAD18^{+/+}$ cells, higher
280 concentrations of TMZ were necessary for synergy with CHK2 or DNA-PKs inhibitors (Figs. 5F-G).
281
282 To validate genetic interactions between *RAD18* and *POLD3,* we inactivated *POLD3* in $RAD18^{+/+}$ and
283 $RAD18^{-/-}$ U373 cells. As shown in Fig. 5H, combined *RAD18* and *POLD3* deletion led to greater-than-
284 additive DNA damage-sensitivity, validating a synthetic lethal relationship.   POLD3 is a component of
285 Polζ and also independently mediates Break Induced Repair (BIR) during Mitotic DNA Synthesis
286 (MiDAS).   In contrast with POLD3-directed sgRNAs, the sgRNAs targeting other Polζ subunit genes
287 dropped out even in the absence of TMZ-treatment (Fig. 5I). However, sgRNAs against other BIR
288 factors showed a dropout pattern similar to POLD3-directed sgRNAs (Fig. 5I). We infer that the role of
289 POLD3 in BIR is important for *RAD18*-deficient GBM to tolerate TMZ. Results of competitive growth
290 assays in Supplementary Fig. 6A&B also demonstrate the effects of deficiencies in FANCD2, PRKDC
291 and POLD3 on TMZ tolerance in U373 cells. Additionally we validate the interactions of RAD18 with
292 POLD3 and CHK2 using U87 GBM cells (Supplementary Fig.6 C&D). Taken together, we show that
293 GBM cells rely on multiple DNA repair pathways to survive TMZ treatment when RAD18 is missing,
294 thereby illustrating the important central role of RAD18 in tolerance of TMZ-induced DNA damage.
295
296 **RAD18 mediates both error-prone and error-free bypass of TMZ-induced DNA lesions**
297
298 We tested the role of *RAD18* in TMZ-induced mutagenesis using U373 cells which readily accumulate
299 O^6mG (and other TMZ-induced lesions) owing to *MGMT* promoter silencing. Moreover, U373 cells
300 harbor *TP53* mutations, and lack growth arrest or apoptotic mechanisms that might otherwise eliminate
301 TMZ-treated cells. Because MMR has also been implicated in hypermutator phenotypes of TMZ-
302 treated gliomas [24,28,30], we also generated $MLH1^{-/-}$ U373 cell lines in $RAD18^{+/+}$ and $RAD18^{-/-}$
303 backgrounds. The resulting U373 cells with individual or combined deficiencies in *RAD18* and *MLH1*
304 and control parental cells were grown for 20 PDs in the presence of TMZ (or DMSO for controls). We
305 isolated and expanded six clones of U373 cells from each genotype and treatment condition (Fig. 6A).
306 Genomic DNA from each of the clones was used to quantify the mutations that arose *de novo* during
307 the course of 20 PDs in the presence or absence of TMZ (Supplementary Table 6).
308

309　As expected, TMZ treatment significantly increased the mean number of total single nucleotide
310　variation (SNV) arising *de novo* in *RAD18*^{+/+} *MLH1*^{+/+} cells (Fig. 6B). In *RAD18*^{-/-} *MLH1*^{+/+} cells, the
311　mean number of total SNV arising basally exceeded the *de novo* basal SNV count of *RAD18*^{+/+} *MLH1*^{+/+}
312　cells. TMZ treatment also led to an increase in the mean SNV count in *RAD18*^{-/-} *MLH1*^{+/+} cells.
313　However, to our surprise, the mean TMZ-induced increase in total SNV was essentially
314　indistinguishable between *RAD18*^{+/+} *MLH1*^{+/+} and *RAD18*^{-/-} *MLH1*^{+/+} cells: TMZ induced 378 SNV in
315　*RAD18*^{-/-} *MLH1*^{+/+} cells and 396 SNV in *RAD18*^{+/+} *MLH1*^{+/+} cells.

317　MMR prevents mutation during DNA replication by removing DNA mismatches from the nascent strand.
318　As expected, all *MLH*^{-/-} cells accumulated more SNV de novo over 20 PDs when compared with their
319　*MLH*^{+/+} counterparts. However, in an *MLH1*^{-/-} background, TMZ only induced a significant number of de
320　novo mutations in *RAD18*^{+/+} cells. In *RAD18*^{-/-} *MLH1*^{-/-} cells there was no significant increase in the
321　number of SNVs following TMZ treatments.   We conclude that RAD18-deficiency leads to an increase
322　in basal mutation rates regardless of MMR status. However, RAD18 contributes to TMZ-induced
323　mutations only in cells with active MMR.

325　We also determined the effect of RAD18 on each of the six possible individual nucleotide substitutions:
326　C>A, C>G, C>T, T>A, T>G, and T>C arising under different experimental conditions. The predominant
327　SNV (C>T) was TMZ-inducible in both *RAD18*^{+/+} and *RAD18*^{-/-} cells (Fig. 6C, Pattern I).   C>T mutations
328　are attributed to error-prone replication of TMZ-induced O^6mG lesions [26,47]. We infer therefore that
329　RAD18 is not involved in error-prone bypass of TMZ-induced O^6mG lesions. However, the five less
330　abundant SNVs not attributable to O^6mG (C>A, C>G, T>A, T>C and T>G) were TMZ-inducible in
331　parental *RAD18*^{+/+}, but not in *RAD18*^{-/-} cells (Fig. 6C, Pattern II).   The results of Fig. 6C showing
332　abrogation of TMZ-induced (C>A, C>G, T>A, T>C and T>G) SNVs in *RAD18*^{-/-} cells suggest that
333　RAD18 is responsible for error-prone bypass of N^7mG and N^3mA lesions. In MMR-deficient *MLH1*^{-/-}
334　cells, the SNV (C>T) was TMZ-inducible in both *RAD18*^{+/+} and *RAD18*^{-/-} genetic backgrounds (Fig. 6D).
335　However, unlike the *MLH1*^{+/+} cells, the other 5 less abundant SNVs were not induced by TMZ in an
336　*MLH1*^{-/-} background (Fig. 6D). Therefore RAD18-mediated error-prone bypass of N^7mG and N^3mA
337　lesions is MMR-dependent.

339　We also determined the impact of *RAD18* and *MLH1* on TMZ-induced COSMIC 'mutation signatures'.
340　As expected from previous studies [26], we observed COSMIC signature 11 only in the mutational
341　portraits of TMZ-treated cells (Fig. 6E, Supplementary Table 7). Interestingly, RAD18-deficiency in
342　MMR-sufficient cells led to an ~2-fold increase in signature 11 counts (Fig. 6F), demonstrating that
343　RAD18 promotes error-free repair of a subset of TMZ-induced DNA lesions (i.e. those arising from
344　O^6mG). However, in an *MLH1*^{-/-} background, RAD18-loss did not lead to further increases in Signature
345　11 counts (Fig. 6F). Therefore, RAD18 suppresses mutagenicity of damaged DNA arising via MMR
346　processing of primary TMZ-induced lesions. Taken together, we show that RAD18-mediated DNA
347　damage tolerance and mutagenesis are dissociable in TMZ-treated GBM: RAD18 mediates tolerance
348　of TMZ-induced DNA damage (Figs. 1-2) and facilitates error-free bypass of the most cytotoxic and
349　mutagenic TMZ-induced lesion (O^6mG). However, RAD18 mediates mutagenesis of N^7mG and N^3mA
350　lesions.

352　**Low RAD18 expression corelates with hypermutation in recurrent GBM patient**

354　We also investigated correlations between *RAD18* and mutation signature 11 in a patient setting. We
355　extracted and quantified signature 11 counts using genomic sequence data from a multi-institute cohort
356　of TMZ-treated recurrent GBM (rGBM) patients (Supplementary Table 8). *RAD18* expression is
357　correlated with proliferation (R=0.75, p=1.7x10^{-14}, Supplementary Fig. 3D). To exclude the impact of
358　proliferation in our analyses of correlation between *RAD18* levels and signature 11 counts, we adjusted
359　the *RAD18* expression level of each sample for proliferation scores, then separated samples into 'high',

360 'medium', and 'low' RAD18 expression groups. Even after controlling for proliferation, hypermutation
361 (sample with >500 counts of Signature 11) was associated with low *RAD18* expression. Consistent with
362 previous reports that MGMT promotor methylation (which suppresses MGMT expression) is associated
363 with TMZ-induced hypermutation [24,29,30], low *RAD18* expression was only associated with
364 hypermutability in MGMT-low samples (Fig. 7A). A logistic regression model was further applied and
365 inferred the potential relationship between adjusted *RAD18* expression and hypermutation (P_{RAD18} =
366 0.014, P_{MGMT} = 0.0436). Our analyses of patient data are consistent with our mutational analyses in
367 cultured cells, and indicate that RAD18 promotes error-free repair of O^6mG lesions, averting TMZ-
368 induced hypermutations (Fig. 7B).
369
370 **DISCUSSION**
371
372 It is increasingly appreciated that neoplastic cells rely on TLS polymerases for diverse gap-filling
373 functions[48]. For example, Polĸ is important for tolerance of ssDNA gaps arising from oncogene-
374 induced DNA replication stress in untransformed mouse and human cells [31]. REV1 is necessary for
375 gap suppression and tolerance of DNA damage from both intrinsic sources and ATR/WEE1-inhibition in
376 ovarian cancer cells [33]. Interestingly, in cisplatin-treated U2OS cells, RAD18, REV1 and POLζ promote
377 gap-filling in G2 while UBC13, RAD51, and REV1-POLζ mediate gap-filling in S-phase [49]. In contrast,
378 we show here that RAD18 and Polĸ are crucial for suppression of TMZ and MMR-induced ssDNA gaps
379 and lethality, while Polι and REV1 are dispensable for DNA damage tolerance in GBM cells. Our
380 finding that Polη-loss promotes TMZ-tolerance is likely explained by previous work showing that Polĸ
381 and Polη are both RAD18-activated and may compete for recruitment to damaged DNA. The PCNA-
382 Interacting Peptide (PIP) box of Polη binds PCNA with higher affinity than the Polĸ PIP motif [50,51].
383 Therefore, the increased TMZ-tolerance of Polη-depleted cells is likely explained by relief of
384 competition for PCNA-binding by Polĸ (the preferred polymerase for repair of TMZ-induced ssDNA).
385 Our study provides entirely new paradigms for how ssDNA arises and is remediated by TLS in the
386 unique setting of TMZ-treated GBM. A recent report by Hanisch et al. also showed that HDAC-
387 overexpressing gliomas become TMZ-tolerant owing to transcriptional induction of RAD18.[52]
388
389 Futile MMR of TMZ-induced O^6mG-thymine mis-pairs activates ATR [53], signaling a G2 checkpoint that
390 protects from TMZ-induced lethality [54,55]. Here we show coordinate activation of CHK1 and RAD18 in
391 response to TMZ-induced DNA damage, consistent with a common RPA/ssDNA-based activation
392 mechanism for both ATR/CHK1 and RAD18 pathways. Moreover, we show that RAD18-deficiency
393 leads to persistent CHK1 phosphorylation, indicating that RAD18-mediated gap-filling eliminates the
394 TMZ-induced ssDNA tracts that trigger ATR/CHK1 signaling. Our CRISPR screen reveals a broad
395 aerial view of the DDR landscape and defines networks deployed by GBM to resist TMZ-induced
396 genotoxicity. sgRNAs targeting FA, HR, and checkpoint signaling pathways were preferentially
397 depleted in TMZ-treated *RAD18*$^{+/+}$ cells, likely indicating that DSB are the ultimate lethal lesions
398 induced by TMZ (Fig. 5D). Through screens with *RAD18*$^{-/-}$ GBM, we identify redundant genome
399 maintenance pathways that serve as back-ups for when RAD18 is absent. FA, NHEJ, checkpoint
400 signaling, and mitosis/spindle assembly checkpoint pathways were preferentially depleted in *RAD18*$^{-/-}$
401 cells, indicating that cells rely on these pathways to process DSB repair when RAD18 is missing (Fig.
402 5E). We also show that the MMR insertion/deletion loop-resolving branch genes MLH3 and MSH3 are
403 synthetically-lethal with RAD18 (Supplementary Fig. 5B). These results indicate that TMZ-induced
404 ssDNA may also be processed to secondary insertion/deletion loop DNA structures in the absence of
405 RAD18-mediated gap-filling (Supplementary Fig. 5C).
406
407 The standard-of-care for GBM includes surgical resection, followed by radiation therapy (RT) plus
408 concomitant and maintenance TMZ chemotherapy [56]. However, patient outcomes remain poor due to
409 various intrinsic resistance mechanisms. NHEJ is the predominant pathway for repair of RT-induced

410   DSBs and confers treatment resistance in GBM [57]. Our CRISPR screen reveals NHEJ as a major
411   backup pathway for tolerance of TMZ-induced DNA damage in *RAD18*^{-/-} cells. Pharmacological
412   inhibition of DNA-PK, or knockout of the *PRKDC* gene increases TMZ-sensitivity of *RAD18*^{-/-} cells.
413   Therefore, co-inhibition of TLS and NHEJ pathways might sensitize GBM cells to standard treatments
414   and improve patient outcomes.
415
416   Our finding that RAD18 is important for tolerance of TMZ-induced DNA damage yet has different
417   mutagenic activities on the distinct TMZ-induced lesions (O^6mG, N^7mG and N^3mA) is highly unexpected
418   and unprecedented. O^6mG is a highly mutagenic DNA lesion [58]. Both high-fidelity replication
419   polymerases and error-prone Y family polymerases can incorporate T across O^6mG *in vitro* [46].
420   However, the DNA polymerase(s) responsible for C>T mutations at O^6mG lesions in cells have not
421   been identified. We show that RAD18 suppresses C>T mutations and cosmic Signature 11 in TMZ-
422   treated GBM. We also show that RAD18 and Polκ perform post-replication filling of MMR-dependent
423   ssDNA gaps. Therefore, we tentatively identify Polκ as the RAD18 effector that performs error-free
424   gap-filling of O^6mG-containing templates, terminating the MMR futile cycle and conferring TMZ-
425   tolerance. Most likely, replicative DNA polymerases (rather than RAD18-dependent TLS polymerases)
426   cause the TMZ-induced C>T mutations that characterize Signature 11. TMZ-induced N^7mG and N^3mA
427   are suspected to be mutagenic [59-61], yet the mechanism of mutagenesis induced by these lesions has
428   been elusive. Our work defines a novel role for RAD18 in error-prone bypass of N^7mG and N^3mA
429   lesions. Mechanistically, RAD18- and MMR-dependent mutations (T>A, C>A, T>C, C>G and T>G)
430   caused by N7mG and N3mA are explained by the results of Pena-Diaz et al.[62]. Those workers
431   demonstrated that DNA replication-independent noncanonical mismatch repair (ncMMR) recruits error-
432   prone TLS polymerases to bypass alkylating DNA lesions. It remains to be determined which RAD18-
433   dependent TLS polymerase(s) mediate error-prone replicative bypass of N^7mG and N^3mA.
434
435   A high mutational burden is found in some glioblastomas, yet the underlying mechanisms of
436   hypermutation are not well understood [23-25]. TMZ treatment has been associated with a specific
437   mutational pattern designated COSMIC mutation signature 11 [26]. A recent study by Touat et al.
438   identified *POLE* or MMR mutations in gliomas harboring hypermutations de novo. In the same study an
439   unbiased screen also identified MMR mutations as likely hypermutation drivers following TMZ treatment
440   [30]. Those authors demonstrated that chronic TMZ-treatment of MMR-deficient patient-derived cell lines
441   (but not isogenic MMR-sufficient controls) induced signature 11 hypermutation [30]. Accordingly, those
442   authors concluded that signature 11 was a result of MMR-deficiency together with TMZ, rather than a
443   'pure' TMZ signature. Similar to the results of Touat et al., we find that mutation signature 11 is TMZ-
444   inducible.   However, in contrast with Touat et al., we show that acquisition of signature 11 is not
445   contingent upon MMR-deficiency. We note that Touat et al. sequenced genomes from heterogeneous
446   pools of tumor cells, whereas we sequence-analyzed genomes from multiple individual clones. Thus
447   the method employed by Touat and colleagues limited their detection of SNVs to substitutions residing
448   in mutational hotspots. The higher resolution of our platform, which reveals any SNV in a clonal
449   sample, explains why we could detect low levels of SNVs even in MMR+ cells. We conclude that
450   signature 11 is a 'pure' TMZ signature that is suppressed by RAD18. MMR-deficiency clearly allows
451   O^6mG:T mismatches to persist and become 'fixed' as G:C> A:T mutations after a second DNA
452   replication cycle (Fig. 7B). Nevertheless, TMZ -induced hypermutation is probably complex and may
453   not be determined solely by TMZ, MGMT and MMR loss. It is likely that multiple additional genetic
454   factors, possibly including other DNA repair pathways, influence hypermutibility.
455
456   Clinical studies also indicate that hypermutation in rGBM is a very complicated problem, whose
457   underlying cause and impact on treatment and patient outcomes remain unclear [25,29,63]. Our analysis of
458   genome sequence data from paired primary and recurrent glioma patient samples shows that low-
459   *RAD18* expression is associated with hypermutation and further hints at a role for RAD18 in
460   suppressing TMZ-induced mutations. Inhibiting RAD18-mediated TLS is a potential therapeutic strategy

461   for sensitizing cancer cells to TMZ-induced lethality, yet will also have significant impact on
462   mutagenesis. Therefore, the relationship between RAD18, DNA damage tolerance, the hypermutator
463   phenotype, and clinical outcome must be clarified in order to validate the RAD18 signaling axis as a
464   therapeutic target pathway.
465

METHODS

Cell lines and gene editing

U373, U87 and LN18 were purchased from the American Type Culture Collection (ATCC). NHA and NHA-RAS cell lines were gifted by Dr. Russell O. Pieper, University of California San Francisco. All cells were grown at 37°C in DMEM medium supplemented with 10% fetal bovine serum and penicillin–streptomycin (1%), in humidified chambers with 5% CO_2. All cell lines tested negative for mycoplasma contamination by MycoAlert Mycoplasma Detection Kit.

Organotype Brain Slice Cultures (OBSC)

All OBSCs were generated from P8 Sprague-Dawley rat pups. Dissected brains were mounted on a vibratome platform submerged in ice-cold BSM. Coronal OBSCs were sliced at a thickness of 300um at ~15 OBSCs/animal. Visibly damaged brains or OBSCs were discarded. Acceptable OBSCs were transferred onto transwell inserts in a 6-well culture plate. 1 mL of brain slice media (BSM), as defined by Satterlee et al. [64] was added under each transwell. The plates were then transferred to a 37°C incubator with 5% CO_2 and 95% humidity. Tumor cells were seeded onto OBSCs 2 h after slicing, with one tumor seeded in the center of each hemisphere for a total of two tumor foci per OBSC. BSM was changed 24h after slicing. Fluorescence images were taken 24 hours post-seeding for normalization of tumor size. Bioluminescence readouts were taken at 96 hours post seeding for assessment of cell viability. Luciferin was added underneath the transwell insert and allowed to incubate for 10 minutes before bioluminescence measurement on an AMI optical imaging system.

Immunoblotting

To prepare extracts containing soluble and chromatin-associated proteins, monolayers of cultured cells typically in 10-cm plates were washed twice in ice-cold PBS and lysed in 200-300 µl of ice-cold cytoskeleton buffer (CSK buffer; 10 mM Pipes, pH 6.8, 100 mM NaCl, 300 mM sucrose, 3 mM $MgCl_2$, 1 mM EGTA, 1 mM dithiothreitol, 0.1 mM ATP, 10 mM NaF, and 0.1% Triton X-100) freshly supplemented with protease inhibitor cocktail and PhosSTOP. Lysates were centrifuged at 4,000 rpm for 4 min to remove the CSK-insoluble nuclei. The detergent-insoluble nuclear fractions were washed once with 300 µl of CSK buffer and then resuspended in a minimal volume of CSK.

For immunoblotting, cell extracts were separated by SDS-PAGE, transferred to nitrocellulose membranes, and incubated overnight with the primary antibodies and 1 hour with the secondary antibodies in 5% nonfat milk TBST. Perkin Elmer Western Lightning Plus ECL was used to develop films.

Plasmids and RNA interference

Plasmid DNA and siRNA oligonucleotides were transfected into U373 cells using electroporation with a GenePulser Xcell (Bio-Rad Laboratories). Electroporation was performed according to the manufacturer's instructions. 200 µl PBS containing 10^7 cells/mL and 1 µM siRNA or 10 µg/ml plasmid DNA was electroporated in a 0.2-cm cuvette using a 150v, 10 ms, and 1 pulse program. SiRNA oligos were transfected into NHA and NHA-RAS cells using Lipofectamine 2000 (Invitrogen) according to the manufacturer's instructions. Sequences of custom siRNA oligonucleotides used in this study can be found in Supplementary Table 9

Adenovirus construction and infection

All adenoviruses were constructed and purified as described previously [65]. In brief, cDNAs encoding RAD18, POLK and POLH with their tags were subcloned into the pAC.CMV shuttle vector.[66] The resulting shuttle vectors were co-transfected with the pJM17 adenovirus plasmid[66] into 293T cells. Recombinant adenovirus clones were isolated by plaque purification and verified by restriction analysis and Southern blotting. The empty vector AdCon (used to control for adenovirus infections) was derived

517   similarly but by co-transfection of the parental pACCMV shuttle vector with pJM17. Adenovirus particles
518   were purified from 293T cell lysates by polyethylene glycol precipitation, CsCl gradient centrifugation,
519   and gel filtration column chromatography. Adenovirus preparations were quantified by A_{260}
520   measurements (OD_{260} 1.0=~10^{12} virus particles). Purified adenovirus was stored at -80°C in small
521   aliquots. U373 cells were infected with 4×10^9 adenovirus particles / mL by direct addition of purified
522   virus to the culture medium.
523
524   **Immunofluorescence microscopy**
525   U373 cells were plated into 4-well chamber slides (5×10^4 cells/well). Adenoviruses were added to the
526   cells 24 h before fixing. Cells were washed 3 times with ice-cold DPBS, then extracted for 5 min in cold
527   CSK buffer on ice surface, washed 3 times with ice-cold DPBS, then fixed for 20 min in -20°C
528   methanol. After 3 washes with DPBS, fixed cells were incubated in blocking buffer (DPBS containing
529   3% BSA and 5% goat serum) for 1 hour, then incubated with primary antibody (diluted 1:200 in blocking
530   buffer) for 2 hours at room temperature. Cells were washed 4 times with DPBS (5min/wash) and
531   incubated 1 hour in blocking buffer containing secondary antibodies (Alexa Fluor 488 Goat anti-Rabbit
532   and Alexa Fluor 555 Goat anti-mouse, 1:400 dilution). Secondary antibody was removed by washing 4
533   times with DPBS and mounted using Fluoro-gel II containing DAPI (1ug/ml) and a coverslip.
534
535   Stained cells were imaged on a Zeiss LSM 710 Spectral Confocal Laser Scanning Microscope (Jena,
536   Germany). We used a Plan-Apochromat 40x/1.40 or 63× /1.40 Oil DIC objective. Excitation lasers
537   were 405 nm (for DAPI), 488 nm (for Alexa Fluor 488), and 543 nm (for Alexa Fluor 555). Emission
538   filter windows were 415–474 (for DAPI), 504–562 (for Alexa Fluor 488), and 504-562 (for Alexa Fluor
539   555). Over 100 nuclei per condition were scored for quantification.
540
541   For acquisition of representative images, we used an Andor Dragonfly Spinning Disk Confocal
542   Microscope (OXFORD Instruments, England) mounted on a Leica DMi8 microscope stand, equipped
543   with an HC PL APO 100x/1.40 OIL CS2 Leica objective. The pinhole size was set to 40 μm. The
544   camera was a Zyla Plus 4.2MP sCMOS with 2048x2048 pixels, with an effective pixel size of 0.063 μm.
545   A piezoelectric Z stage was used to acquire Z stacks at 0.2 um intervals. Excitation lasers were
546   405 nm (for DAPI), 488 nm (for Alexa Fluor 488), and 561 nm (for Alexa Fluor 555). Emission filters
547   were 445/46 (for DAPI), 521/38 (for Alexa Fluor 488), and 594/43 (for Alexa Fluor 555). Images were
548   deconvolved in Fusion/Autoquant (version XYZ) using XYZ settings.
549
550   For live cell imaging, U373 cells were plated into 4-well glass bottom chamber slides (5×10^4 cells/well).
551   TMZ (20 μM) was diluted in culture media and directly added to wells. Adenovirus (AdGFP-Polκ or
552   AdYFP-Pol) was added into culture media 24 hours before imaging. An Andor XD Spinning Disk
553   Confocal Microscope system with Tokai Hit incubator climate control was used for image acquisition. A
554   Hamamatsu Flash4v2 sCMOS camera with 20X/0.75 UPlan S-APO Olympus objective was selected for
555   higher resolution and wider view. FITC and brightfield channels were selected for acquisition. Over 150
556   cells per condition were manually scored for nuclear foci using the ImageJ cell counter plug-in.
557
558   **Flow cytometry**
559
560   *BrdU incorporation assay*
561   Growing cells were incubated with 10 μM BrdU for one hour before trypsinization. Trypsinized cells
562   were suspended in 65% PBS with 35% ethanol, and fixed overnight at 4°C. Fixed cells were denatured
563   using HCl and then neutralized with borax before stained with fluorescent anti-BrdU antibodies for an
564   hour, exactly as described previously [65] . Nuclei were incubated in PBS containing 10 μg/mL of
565   propidium iodide (PI) and 40 μg/mL of RNaseA for 1 hour. Stained cells were analyzed using an Accuri
566   C6 plus flow cytometer (BD) and analyzed using the manufacturer's software.

567

G2/M cell cycle assay

Trypsinized cells were resuspended in 1 mL PTEMF buffer (chromatin extraction, fixation and permeabilization, 20 mM PIPES pH 6.8, 10 mM EGTA, 0.2% Triton X-100, 1 mM MgCl2 and 4% formaldehyde) and incubated for 20 min. 5 mL DPBS was added to quench the PTEMF buffer. Fixed cells were resuspended in 1 mL blocking buffer (DPBS+1%BSA+0.1% NP-40) and incubated for 1 hour before addition of primary antibodies (Mitosin, 1:200; pH3 1:400 in100 μL blocking buffer) and overnight incubation at 4 °C. Primary antibodies were washed using blocking buffer and cells were incubated in secondary antibodies (Alexa 488 anti-Mouse, 1:400; Alexa 647 anti-Rabbit in 100 μL blocking buffer) for 1 hour at in the dark. After washing in blocking buffer to remove secondary antibodies, cells were re-suspended in blocking buffer containing 10 μg/mL PI and 40 μg/mL RNase A and incubated at 4 °C overnight. Stained cells were analyzed by flow cytometry on an Accuri C6 plus flow cytometer (BD) and analyzed using the manufacturer's software.

pRPA32s33 and γH2AX staining

Trypsinized cells were resuspended in 1 mL PTEMF buffer and incubated for 20 min. 5mL DPBS was added to quench the PTEMF buffer. Fixed cells were resuspended in 1 mL blocking buffer, then incubated for 1 hour before adding primary antibodies (pRPA32s33, 1:200; γH2AX 1:400) in100 μL blocking buffer. After incubating overnight at 4°C, primary antibodies were removed by washing in blocking buffer. Then, cells were incubated in secondary antibodies (Alexa 488 anti-Mouse, 1:400; Alexa 647 anti-Rabbit) in 100 μL blocking buffer for 1 hour in the dark. Secondary antibodies were removed by washing in blocking buffer. Then, cells were resuspended in blocking buffer containing 10 μg/mL PI and 40 μg/mL RNase A and incubated at 4°C overnight. Stained cells were analyzed by flow cytometry on an Accuri C6 plus flow cytometer (BD).

O^6mG quantification

LN18 *RAD18*^{+/+} and *RAD18*^{-/-} cells were pre-treated with 100 mM O^6bG for 3 hours then co-incubated with 200 μM TMZ + 20 mM O^6bG or 200 μM TMZ alone for the indicated times. Genomic DNA was then purified from the cells and used to measure O^6mG lesions. The experimental procedure and instrument parameters for O^6mG quantification were similar to those described in previous reports [67-69] with minor modifications. Briefly, the purified DNA samples were spiked with 12.5 fmol $[^{15}N_5]O^6mG$, enzymatically digested with DNAse I (200 units), alkaline phosphatase (5 units), and phosphodiesterase (0.005 units) at 37°C for 1 hr, and fractionated with an off-line HPLC after size-exclusion removal of the digesting enzymes. The purified O^6mG and $[^{15}N_5]O^6mG$ were dried, reconstituted with 14 μL 0.1% formic acid in water, and injected (6 μL per injection) to the nanoLC-ESI-MS/MS system for quantitation of O^6mG. The quantitating and major product ions of O^6mG and $[^{15}N_5]O^6mG$ were produced by the neutral loss of deoxyribose moiety from each corresponding precursor. Based upon the known spiked internal standard prior to DNA digestion and the signal ratio of O^6mG : $[^{15}N_5]O^6mG$, the amount of O^6mG in samples can be estimated, then normalized to the dG content (recorded from the HPLC-UV analysis) in units of adducts/dG.

Gene editing

Oligonucleotides encoding sgRNAs targeting specific genes or non-targeting control sgRNAs (see Supplemental data 'Oligo sequences') were cloned into LentiCRISPRv2 vector [70] which was a gift from Feng Zhang (Addgene plasmid # 52961). The resulting vectors were transformed into Endura Chemically Competent Cells according to the manufacturer's protocol. To generate lentiviruses for gene editing, LentiCRISPRv2-based vectors were mixed with helper plasmids pMD2.G and pSPAX2 [71], gifts from Didier Trono (Addgene # 12259 and 12260) using a 4:1:3 ratio (12 μg DNA per transfection reaction) and co-transfected into low-passage HEK 293T cells using Lipofectamine 2000. Lentivirus-

616   containing culture medium from transfected cells was collected at 24 h and 48 h, filtered through 0.45
617   μm filter, then aliquoted and stored at −80°C.
618
619   **Viability assays**
620   Cells were seeded at densities of 1000 cells/well (NHA, NHA-RAS), 1500 cells/well (U87, U373), or
621   2000 cells/ well (LN18) in triplicate in 6-well plates. All drugs (TMZ, MeOX, CHK2i DNA-PKi) were
622   diluted in growth medium from stock solutions and added directly to the cells. In most experiments, the
623   cell culture medium was replenished with fresh drug every day for 5 days. However, for siRNA
624   knockdown experiments, drugs were replenished twice daily for 2 days beginning 24 hours after
625   transfection (thereby ensuring that cells only received drug at times following knockdown of target
626   mRNAs). For the O6bG co-treatment experiments, LN18 cells were pretreated with 100 μM O6bG 3
627   hours before the first treatment 20 μM O6bG + TMZ. To visualize colonies, culture plates were stained
628   with 0.05% crystal violet in 1× PBS containing 1% methanol and 1% formaldehyde ~12 days after cell
629   seeding. The plates were scanned using an Epson perfection V800 scanner set to 'positive film' mode.
630
631   **Single-cell RNA-seq data analysis**
632   Smart-seq2 single-cell RNA-seq data generated using malignant GBM cells were obtained from
633   GSM3828672 [43]. Data normalization and pre-processing were performed using the Seurat workflow [72].
634   Batch correction was performed using R package harmony [73]. Cell-cycle scores of individual cells were
635   assigned using Seurat::CellCycleScoring() based on the curated list Seurat::cc.genes.updated.2019
636   comprising cell cycle markers.
637
638   **Defining relationships between RAD18 expression and the TMZ mutation signature using a GBM**
639   **patient cohort**
640   The integrated GBM cohort containing bulk RNA-seq data, whole exome sequencing data and clinical
641   information was obtained from the published work of Wang et al. [24]. Data from POLE-mutated samples
642   were excluded from analysis based on previous work implicating POLE alterations in GBM
643   hypermutation [30]. GSVA was performed to score the degree of proliferation based on cell-cycle marker
644   genes from Seurat::cc.genes.updated.2019 [74]. MutationalPatterns::fit_to_signatures() was used to
645   reconstruct the mutation matrix and evaluate the mutation counts contributed by Signature 11 based on
646   the COSMIC mutational signatures v2 [26]. Linear regression analysis was performed by function
647   lm(RAD18 ~ Proliferation_Score), and difference between RAD18 expression and expected RAD18
648   expression was taken as adjusted RAD18 expression to reduce the contribution brought by high
649   proportion of proliferating cells. According to the adjusted RAD18 expression level, we divided the
650   patient into 'high', 'medium' and 'low' groups. The logistic regression model on Wang cohort was
651   created using function glm(Hypermutation ~ RAD18_adj + MGMT) with parameter
652   family=binomial(link='logit'), and P values of variables associated with z values in the model were used
653   to measure the significance of their latent contribution to hypermutation.
654
655   **Generating Cell lines for CRISPR screen and mutagenesis assay**
656   For the CRISPR-Cas9 screens and mutagenesis assay, we generated isogenic clonal *RAD18*$^{-/-}$ and
657   *RAD18*$^{+/+}$ cell lines by transducing parental U373 cells with a RAD18-directed sgRNA or with a non-
658   targeting sgRNA respectively.
659
660   In brief, a LentiCRISPRv2-DD-Cas9-BSD vector (generated in-house, Supplementary Fig. 7) encoding
661   sgRAD18 or a non-targeting sgRNA was transduced into U373 cells by electroporation. Transfected
662   cells were selected by growth in blasticidin (10 μg/mL) for 4 days and then additionally treated with
663   Shield-1 (1 μM) for another 6 days. Single clones of blasticidin-resistant and Shield-1-treated cells
664   were isolated, expanded and tested for *RAD18* disruption by TIDE assay (https://tide.nki.nl/) and

665 western. The clonal U373 *RAD18*$^{-/-}$ and *RAD18*$^{+/+}$ cell lines thus obtained were verified lentivirus
666 cassette-free based upon blasticidin-sensitivity.
667
668

CRISPR-Cas9 loss-of-function screen
670 The DDR-CRISPR lentivirus library comprises 5040 sgRNAs targeting 504 DDR genes (10
671 independent sgRNAs per gene), and 1000 non-targeting control sgRNAs (Supplementary Table 1).
672 Each domain-focused sgRNA(20nt) is flanked by 5' and a 3' universal flanking sequence
673 (Supplementary Fig. 7). The oligonucleotide pool encoding sgRNAs in the library was synthesized by
674 CustomArray Inc. The DDR-CRISPR library was PCR amplified using 017_ArrayF and 018_ArrayR
675 primers (Supplementary Table 9) with Q5 High-Fidelity polymerase. The amplified library DNA was
676 purified using a MinElute PCR purification kit and was cloned into LentiCRISPRv2-DD-Cas9-BSD via
677 NEBuilder HiFi DNA Assembly. The resulting HiFi assembly mixture was transduced into Endura
678 Electrocompetent Cells using a Gene Pulser Xcell electroporator in 1 mm cuvette with 1800 Volts, 10
679 µFarad, 600 Ohm program. 6 electroporation reactions were performed to ensure high coverage of the
680 entire library. After a 1 h incubation at 37°C, transformed bacteria were plated on twelve 15 cm LB
681 ampicillin plates and incubated overnight at 37°C. Next, 10 mL of LB was added to each plate and the
682 transformed bacterial colonies were recovered using sterile scrapers. Pooled bacterial colonies from 3
683 plates were transferred to 500 mL LB and grown with shaking at 37 °C for 3 hours. The resulting
684 bacterial cultures were collected and DDR-CRISPR library plasmid DNA was purified using a Qiagen
685 plasmid DNA maxiprep kit.
686

Lentivirus generation
688 Low-passage HEK 293T cells in 150 mm dishes were grown to 70-90% confluence and transfected
689 using a PEI-based method. Briefly, for each transfection reaction purified plasmid DNAs (4µg pMD2.G,
690 6µg pSPAX2 and 8µg Library plasmid) were diluted in 1 mL serum-free DMEM and mixed gently.
691 Then, 80 µL PEI was added to the DNA-DMEM solution, mixed gently, and incubated for 20 minutes at
692 room temperature. The resulting DNA-DMEM-PEI solution was added dropwise to 293T cells, which
693 were then returned to the incubator overnight. The next day, transfection medium was removed and
694 replaced with 18mL fresh complete medium. Virus-containing cell culture medium was collected 24 h
695 later. Cells were given another 18 mL of fresh medium and virus was collected again 48 h post-
696 transfection. Virus-containing medium was filtered through a 0.45µm filter, then aliquoted and stored at
697 −80°C.
698
699

CRISPR-Cas9 screens with DDR CRISPR library
701 The DDR CRISPR Library lentivirus was transduced into U373 *RAD18*$^{+/+}$ or U373 *RAD18*$^{-/-}$ cells, at an
702 MOI of ~0.3. 48 h after lentiviral infection, stably-transduced cells were selected in blasticidin (10
703 µg/mL) for 4 days followed by 2 days of treatment with shield-1(1 µM). At this time point, 2 million cells
704 were collected and frozen for control 'PD0' samples. Remaining cells were then replated and cultured
705 in the presence of TMZ or with DMSO (for the control group). U373 *RAD18*$^{+/+}$ and U373 *RAD18*$^{-/-}$ cells
706 were treated daily with 4 µM and 2 µM TMZ respectively (doses corresponding to the IC$_{20}$ for each cell
707 line). Shield-1 was maintained in the growth medium for 4 days after the PD0 time point. Every 2-3
708 days cells were passaged by reseeding 1.6×10^6 cells into two 15 cm plates (thereby maintaining >250-
709 fold representation of each sgRNA in the library). Using this culture regimen, U373 *RAD18*$^{+/+}$ and U373
710 *RAD18*$^{-/-}$ cells were grown in the presence or absence of TMZ for 20 population doublings (PD20).
711 Three independent screens were performed. Genomic DNA was extracted from all PD0 and PD20
712 samples and a two-step PCR was performed to amplify sgRNAs. In the first PCR step, 5 µg gDNA per
713 experimental group (U373 *RAD18*$^{+/+}$ +/- TMZ, U373 *RAD18*$^{-/-}$ +/- TMZ) was used as a template to
714 achieve ~120 × coverage of the DDR CRISPR library. Five 50 µL PCR reactions were performed for

715   each experimental group and each reaction contained 1 μg gDNA, NEB Q5 Hot Start polymerase
716   (added as a 2x master mix), with primer 1st_lib_F_mix and 1st_lib_R (Supplementary Table 9). The
717   product was purified using AMPure XP beads. A second PCR step was used to add indexed
718   sequencing adapters. Each secondary PCR reaction contained 1 ng of purified PCR product from the
719   first PCR step as template in a 50 μL reaction volume containing indexing primers (Supplementary
720   Table 9). After purification using AMPure XP beads, the 320 bp products were quantified using Qubit
721   and diluted to 1ng/μL, then sequenced using HiSeq 4000, PE 2x150 (Novogene Co).
722
723   *Analysis of sequencing data*
724   FASTQ sequence files were analyzed with PinAPL-Py (http://pinapl-py.ucsd.edu/) [75]. Briefly, sgRNA
725   counts of PD20 samples relative to PD0 were compared for all experimental groups to determine
726   sgRNA abundance changes that occurred over 20 population doublings. The SUMLFC (the sum of log
727   fold-changes of all sgRNAs targeting the same gene, SigmaFC) algorithm was selected for gene
728   ranking. The DDR pathways heatmap in Fig. 5D was plotted by grouping the sgRNAs according to
729   their corresponding DDR pathways (Supplementary Table 4). Log10 was applied to sgRNA counts to
730   convert data sets to normal distribution. A Paired two-samples t test p value representing the drop out
731   level of PD20 vs PD0 log10 (counts). -log10 (p value) was used to generate the heatmap
732   (Supplementary Table 5). We used the fmsb (version 0.7.3) package in R (version 4.1.2) to make the
733   radar chart. For each cell line and each pathway, we individually performed a two-sided Z-test on the
734   null hypothesis that the genes in the pathway are not on average different in dropouts. The test statistic
735   was calculated as follows. First, using the normalized read counts from PinAPL-Py (Supplementary
736   Table 2), we obtained the ratios between PD20 and PD0 for each guide and log2-transformed them.
737   Then for each gene g, we constructed a two-sample Z-statistic comparing TMZ to DMSO as:

738
$$Z_g = \frac{X_g}{S_g}$$

739   where X_g is the difference in sample means and S_g is the corresponding standard deviation.
740   Finally, we combined the gene-specific Z-statistics in each pathway P as:

741
$$Z_P = \frac{\sum_{g \in P} X_g}{\sqrt{\sum_{g \in P} S_g^2}}$$

742   which follows a standard normal distribution under the null hypothesis.
743
744
745   **Mutagenesis assay**
746   U373 $RAD18^{+/+}$ and U373 $RAD18^{-/-}$ cells were infected with lentiCRISPR virus targeting the *MLH1*
747   gene, or with a lentivirus encoding a non-targeting control sgRNA. Stably-transduced cells were
748   selected in puromycin (2 μg/ml). Pools of the resulting U373 cells ($RAD18^{+/+}MLH1^{+/+}$, $RAD18^{+/+}MLH1^{-/-}$,
749    $RAD18^{-/-}MLH1^{+/+}$ and $RAD18^{-/-}MLH1^{-/-}$) were seeded into 10 cm plates (5 x 10^5 cells/plate) and cultured
750   in the presence of 4μM TMZ (or DMSO for control groups) for 20 population doublings (PD20). Single
751   cells were isolated from each treatment group and expanded into clones that were analyzed via TIDE
752   assay and immunoblot to confirm *RAD18* and *MLH1* genotypes. Expanded cells containing partially-
753   edited clones, or multi-clonal populations were discarded. For each genotype and TMZ treatment
754   condition, six validated clonal cell populations were expanded. Genomic DNA from each clonal line
755   was subject to whole-exome sequencing using NovaSeq 6000 PE150 (Novogene Co).
756   For all FASTQ sequence files, we firstly discarded reads below the 50 bases long and reads with
757   insufficient base qualities using Trimmomatic 0.39[76]. Next, the trimmed sequencing reads were mapped
758   to the homo sapiens reference genome (assembly GRCh37/hg19) using BWA-MEM alignment
759   algorithm in BWA package (version 0.7.17)[77]. Then we converted the resulting sequence alignment
760   map (SAM) files to binary alignment map (BAM) files using Picard 2.23.4

761 (http://broadinstitute.github.io/picard). After sorting the BAM files by SAMtools 1.11[78], we removed
762 duplicates and validated the postprocessed BAM files using Picard again.
763 To call single nucleotide variant (SNV), a base quality score recalibration was performed by using the
764 tools IndexFeatureFile, BaseRecalibrator, and ApplyBQSR in GATK 4.1.9.0[79]. Known simple nucleotide
765 polymorphisms (dbSNP Build 151) reported in the GRCh37/hg19 background by NCBI
766 (https://ftp.ncbi.nih.gov/snp/organisms/human_9606_b151_GRCh37p13/VCF/common_all_20180423.v
767 cf.gz) were removed as one step in the base quality score recalibration. After the recalibration
768 procedure, we supply the BAM files prepared for substitution-calling to the Mutect2 tool of GATK
769 4.1.9.0[79] to generate variant calling format (VCF) files. Subsequently, we removed probable technical or
770 germline artifacts by using FilterMutectCalls tool of GATK. To further reduce false-positive callings, we
771 conducted three additional procedures: 1. we filtered out all INDELs that are greater than 10 bps by
772 using SelectVariants of GATK; 2. using filter tool of SnpSift 4.3t[80], we applied additional filters for
773 mutant allele frequency (≥10%), coverage (≥10×) at particular positions in tumor and normal samples,
774 and number of supporting reads (≥3) for the mutation in the tumor samples; 3. we compare the SNVs
775 and indels to known polymorphisms (U373 MG glioblastoma) using the bcftools in SAMtools. Thus, we
776 obtain the somatic mutations. In addition, we mapped the mutation calls in the filtered VCF files to the
777 protein coding exon region database (https://earray.chem.agilent.com/suredesign/), and removed the
778 mutations that are not overlapped with any regions in Agilent SureSelect DNA - SureSelect Human All
779 Exon V6 (Supplementary Fig. 8).
780
781 **Image quantitation**
782 For clonogenic survival assays, stained plates were scanned and the ImageJ plugin ColonyArea was
783 used to automatically quantify colonies [81]. A threshold of 200 was manually applied to all experiments.
784 Colony survival in treated experimental groups was normalized to untreated controls. For chemical
785 inhibitor studies, synergy distribution heatmaps were generated by SynergyFinder web application
786 (Version 3.0) (https://synergyfinder.fimm.fi/) [82]. To quantify cells containing CFP-RAD18 nuclear foci,
787 and co-localization of GFP-Polκ/PCNA foci, composite images acquired using a Zeiss LSM 710
788 microscope were generated using Fiji to overlay multiple channels. Cells positive for single foci were
789 counted manually. Cells containing co-localizing foci were identified and enumerated using the cell
790 counter plug-in. To quantify CFP-RAD18/RPA32 percentage overlap, images acquired by an Andor
791 Dragonfly Spinning Disk Confocal Microscope were analyzed using Imaris Microscopy Image Analysis
792 Software (Imaris 9.9). The percentage of surfaces overlap volume to surface of CFP-RAD18 channel
793 was used to enumerate the CFP-RAD18/RPA32 overlap. For live cell imaging, the images acquired by
794 Andor XD Spinning Disk Confocal Microscope were opened in Fiji, and foci-positive cells were manually
795 counted using the cell counter plug-in.
796
797 The post-hoc Tukey HSD (Honestly Significant Difference) test and multiple unpaired t test were used
798 to calculate the p value for experiments with multiple treatment groups.
799
800 **DATA AVAILABILITY**
801 Data can be accessed through http://www.ncbi.nlm.nih.gov/bioproject/901961
802
803 **CODE AVAILABILITY**
804 Code will be made available by https://github.com/jitonglou/RAD18_TMZ_data and
805 https://github.com/CHENGHAO-WANG/radarChart/tree/main
806
807
808
809 **REFERENCES**
810

811   1   Chinot, O. L. *et al.* Bevacizumab plus radiotherapy-temozolomide for newly diagnosed
812   glioblastoma. *The New England journal of medicine* **370**, 709-722, doi:10.1056/NEJMoa1308345
813   (2014).

814   2   Johnson, D. R. & O'Neill, B. P. Glioblastoma survival in the United States before and during the
815   temozolomide era. *J Neurooncol* **107**, 359-364, doi:10.1007/s11060-011-0749-4 (2012).

816   3   Newlands, E. S., Stevens, M. F., Wedge, S. R., Wheelhouse, R. T. & Brock, C. Temozolomide: a
817   review of its discovery, chemical properties, pre-clinical development and clinical trials. *Cancer*
818   *treatment reviews* **23**, 35-61, doi:10.1016/s0305-7372(97)90019-0 (1997).

819   4   Dianov, G. L., Sleeth, K. M., Dianova, II & Allinson, S. L. Repair of abasic sites in DNA. *Mutat Res*
820   **531**, 157-163, doi:10.1016/j.mrfmmm.2003.09.003 (2003).

821   5   Margison, G. P., Santibanez Koref, M. F. & Povey, A. C. Mechanisms of
822   carcinogenicity/chemotherapy by O6-methylguanine. *Mutagenesis* **17**, 483-487,
823   doi:10.1093/mutage/17.6.483 (2002).

824   6   Butler, M. *et al.* MGMT Status as a Clinical Biomarker in Glioblastoma. *Trends Cancer* **6**, 380-
825   391, doi:10.1016/j.trecan.2020.02.010 (2020).

826   7   Yu, W., Zhang, L., Wei, Q. & Shao, A. O(6)-Methylguanine-DNA Methyltransferase (MGMT):
827   Challenges and New Opportunities in Glioma Chemotherapy. *Front Oncol* **9**, 1547,
828   doi:10.3389/fonc.2019.01547 (2019).

829   8   Karran, P. & Marinus, M. G. Mismatch correction at O6-methylguanine residues in E. coli DNA.
830   *Nature* **296**, 868-869, doi:10.1038/296868a0 (1982).

831   9   Goldmacher, V. S., Cuzick, R. A., Jr. & Thilly, W. G. Isolation and partial characterization of
832   human cell mutants differing in sensitivity to killing and mutation by methylnitrosourea and N-
833   methyl-N'-nitro-N-nitrosoguanidine. *J Biol Chem* **261**, 12462-12471 (1986).

834   10   Kat, A. *et al.* An alkylation-tolerant, mutator human cell line is deficient in strand-specific
835   mismatch repair. *Proc Natl Acad Sci U S A* **90**, 6424-6428, doi:10.1073/pnas.90.14.6424 (1993).

836   11   Noonan, E. M., Shah, D., Yaffe, M. B., Lauffenburger, D. A. & Samson, L. D. O6-Methylguanine
837   DNA lesions induce an intra-S-phase arrest from which cells exit into apoptosis governed by
838   early and late multi-pathway signaling network activation. *Integr Biol (Camb)* **4**, 1237-1255,
839   doi:10.1039/c2ib20091k (2012).

840   12   Quiros, S., Roos, W. P. & Kaina, B. Processing of O6-methylguanine into DNA double-strand
841   breaks requires two rounds of replication whereas apoptosis is also induced in subsequent cell
842   cycles. *Cell Cycle* **9**, 168-178, doi:10.4161/cc.9.1.10363 (2010).

843   13   Duckett, D. R., Bronstein, S. M., Taya, Y. & Modrich, P. hMutSalpha- and hMutLalpha-dependent
844   phosphorylation of p53 in response to DNA methylator damage. *Proc Natl Acad Sci U S A* **96**,
845   12384-12388, doi:10.1073/pnas.96.22.12384 (1999).

846   14   Yoshioka, K., Yoshioka, Y. & Hsieh, P. ATR kinase activation mediated by MutSalpha and
847   MutLalpha in response to cytotoxic O6-methylguanine adducts. *Mol Cell* **22**, 501-510,
848   doi:10.1016/j.molcel.2006.04.023 (2006).

849   15   Kaina, B., Christmann, M., Naumann, S. & Roos, W. P. MGMT: key node in the battle against
850   genotoxicity, carcinogenicity and apoptosis induced by alkylating agents. *DNA Repair (Amst)* **6**,
851   1079-1099, doi:10.1016/j.dnarep.2007.03.008 (2007).

852   16   Karran, P. & Bignami, M. DNA damage tolerance, mismatch repair and genome instability.
853   *Bioessays* **16**, 833-839, doi:10.1002/bies.950161110 (1994).

854 17 Olivera Harris, M. *et al.* Mismatch repair-dependent metabolism of O6-methylguanine-
855   containing DNA in Xenopus laevis egg extracts. *DNA Repair (Amst)* **28**, 1-7,
856   doi:10.1016/j.dnarep.2015.01.014 (2015).
857 18 York, S. J. & Modrich, P. Mismatch repair-dependent iterative excision at irreparable O6-
858   methylguanine lesions in human nuclear extracts. *J Biol Chem* **281**, 22674-22683,
859   doi:10.1074/jbc.M603667200 (2006).
860 19 Li, G. M. Mechanisms and functions of DNA mismatch repair. *Cell research* **18**, 85-98,
861   doi:10.1038/cr.2007.115 (2008).
862 20 Gupta, D. & Heinen, C. D. The mismatch repair-dependent DNA damage response: Mechanisms
863   and implications. *DNA Repair (Amst)* **78**, 60-69, doi:10.1016/j.dnarep.2019.03.009 (2019).
864 21 Kaina, B. & Christmann, M. DNA repair in personalized brain cancer therapy with temozolomide
865   and nitrosoureas. *DNA Repair (Amst)* **78**, 128-141, doi:10.1016/j.dnarep.2019.04.007 (2019).
866 22 Lonardi, S., Tosoni, A. & Brandes, A. A. Adjuvant chemotherapy in the treatment of high grade
867   gliomas. *Cancer treatment reviews* **31**, 79-89, doi:10.1016/j.ctrv.2004.12.005 (2005).
868 23 Brennan, C. W. *et al.* The somatic genomic landscape of glioblastoma. *Cell* **155**, 462-477,
869   doi:10.1016/j.cell.2013.09.034 (2013).
870 24 Wang, J. *et al.* Clonal evolution of glioblastoma under therapy. *Nat Genet* **48**, 768-776,
871   doi:10.1038/ng.3590 (2016).
872 25 Barthel, F. P. *et al.* Longitudinal molecular trajectories of diffuse glioma in adults. *Nature* **576**,
873   112-120, doi:10.1038/s41586-019-1775-1 (2019).
874 26 Alexandrov, L. B. *et al.* Signatures of mutational processes in human cancer. *Nature* **500**, 415-
875   421, doi:10.1038/nature12477 (2013).
876 27 Cancer Genome Atlas Research, N. Comprehensive genomic characterization defines human
877   glioblastoma genes and core pathways. *Nature* **455**, 1061-1068, doi:10.1038/nature07385
878   (2008).
879 28 Johnson, B. E. *et al.* Mutational analysis reveals the origin and therapy-driven evolution of
880   recurrent glioma. *Science* **343**, 189-193, doi:10.1126/science.1239947 (2014).
881 29 Mathur, R. *et al.* MGMT promoter methylation level in newly diagnosed low-grade glioma is a
882   predictor of hypermutation at recurrence. *Neuro-oncology* **22**, 1580-1590,
883   doi:10.1093/neuonc/noaa059 (2020).
884 30 Touat, M. *et al.* Mechanisms and therapeutic implications of hypermutation in gliomas. *Nature*
885   **580**, 517-523, doi:10.1038/s41586-020-2209-9 (2020).
886 31 Yang, Y. *et al.* DNA repair factor RAD18 and DNA polymerase Polkappa confer tolerance of
887   oncogenic DNA replication stress. *J Cell Biol*, doi:10.1083/jcb.201702006 (2017).
888 32 Yang, Y. *et al.* Diverse roles of RAD18 and Y-family DNA polymerases in tumorigenesis. *Cell*
889   *Cycle*, 1-11, doi:10.1080/15384101.2018.1456296 (2018).
890 33 Nayak, S. *et al.* Inhibition of the translesion synthesis polymerase REV1 exploits replication gaps
891   as a cancer vulnerability. *Sci Adv* **6**, eaaz7808, doi:10.1126/sciadv.aaz7808 (2020).
892 34 Hedglin, M. & Benkovic, S. J. Regulation of Rad6/Rad18 Activity During DNA Damage Tolerance.
893   *Annual review of biophysics* **44**, 207-228, doi:10.1146/annurev-biophys-060414-033841 (2015).
894 35 Tsuji, Y. *et al.* Recognition of forked and single-stranded DNA structures by human RAD18
895   complexed with RAD6B protein triggers its recruitment to stalled replication forks. *Genes Cells*
896   **13**, 343-354 (2008).

897   36   Davies, A. A., Huttner, D., Daigaku, Y., Chen, S. & Ulrich, H. D. Activation of ubiquitin-dependent
898   DNA damage bypass is mediated by replication protein a. *Mol Cell* **29**, 625-636 (2008).

899   37   Ulrich, H. D. How to activate a damage-tolerant polymerase: consequences of PCNA
900   modifications by ubiquitin and SUMO. *Cell Cycle* **3**, 15-18 (2004).

901   38   Sonoda, Y. *et al.* Formation of intracranial tumors by genetically modified human astrocytes
902   defines four pathways critical in the development of human anaplastic astrocytoma. *Cancer Res*
903   **61**, 4956-4960 (2001).

904   39   Trivedi, R. N., Almeida, K. H., Fornsaglio, J. L., Schamus, S. & Sobol, R. W. The role of base
905   excision repair in the sensitivity and resistance to temozolomide-mediated cell death. *Cancer*
906   *Res* **65**, 6394-6400, doi:10.1158/0008-5472.CAN-05-0715 (2005).

907   40   Liu, L. & Gerson, S. L. Therapeutic impact of methoxyamine: blocking repair of abasic sites in the
908   base excision repair pathway. *Curr Opin Investig Drugs* **5**, 623-627 (2004).

909   41   Liu, L., Taverna, P., Whitacre, C. M., Chatterjee, S. & Gerson, S. L. Pharmacologic disruption of
910   base excision repair sensitizes mismatch repair-deficient and -proficient colon cancer cells to
911   methylating agents. *Clin Cancer Res* **5**, 2908-2917 (1999).

912   42   Satterlee, A. B., Dunn, D. E., Lo, D. C., Khagi, S. & Hingtgen, S. Tumoricidal stem cell therapy
913   enables killing in novel hybrid models of heterogeneous glioblastoma. *Neuro-oncology* **21**,
914   1552-1564, doi:10.1093/neuonc/noz138 (2019).

915   43   Neftel, C. *et al.* An Integrative Model of Cellular States, Plasticity, and Genetics for
916   Glioblastoma. *Cell* **178**, 835-849 e821, doi:10.1016/j.cell.2019.06.024 (2019).

917   44   D'Atri, S. *et al.* Involvement of the mismatch repair system in temozolomide-induced apoptosis.
918   *Molecular pharmacology* **54**, 334-341, doi:10.1124/mol.54.2.334 (1998).

919   45   Wojtaszek, J. L. *et al.* A Small Molecule Targeting Mutagenic Translesion Synthesis Improves
920   Chemotherapy. *Cell* **178**, 152-159 e111, doi:10.1016/j.cell.2019.05.028 (2019).

921   46   Haracska, L., Prakash, S. & Prakash, L. Replication past O(6)-methylguanine by yeast and human
922   DNA polymerase eta. *Molecular and cellular biology* **20**, 8001-8007 (2000).

923   47   Alexandrov, L. B., Nik-Zainal, S., Wedge, D. C., Campbell, P. J. & Stratton, M. R. Deciphering
924   signatures of mutational processes operative in human cancer. *Cell reports* **3**, 246-259,
925   doi:10.1016/j.celrep.2012.12.008 (2013).

926   48   Anand, J. *et al.* Roles of trans-lesion synthesis (TLS) DNA polymerases in tumorigenesis and
927   cancer therapy. *NAR Cancer* **5**, zcad005, doi:10.1093/narcan/zcad005 (2023).

928   49   Tirman, S. *et al.* Temporally distinct post-replicative repair mechanisms fill PRIMPOL-dependent
929   ssDNA gaps in human cells. *Mol Cell* **81**, 4026-4040 e4028, doi:10.1016/j.molcel.2021.09.013
930   (2021).

931   50   Hishiki, A. *et al.* Structural basis for novel interactions between human translesion synthesis
932   polymerases and proliferating cell nuclear antigen. *J Biol Chem* **284**, 10552-10560,
933   doi:10.1074/jbc.M809745200 (2009).

934   51   Durando, M., Tateishi, S. & Vaziri, C. A non-catalytic role of DNA polymerase eta in recruiting
935   Rad18 and promoting PCNA monoubiquitination at stalled replication forks. *Nucleic Acids Res*,
936   doi:10.1093/nar/gkt016 (2013).

937   52   Hanisch, D. *et al.* Class I HDAC overexpression promotes temozolomide resistance in glioma
938   cells by regulating RAD18 expression. *Cell Death Dis* **13**, 293, doi:10.1038/s41419-022-04751-7
939   (2022).

940   53   Ganesa, S., Sule, A., Sundaram, R. K. & Bindra, R. S. Mismatch repair proteins play a role in ATR
941   activation upon temozolomide treatment in MGMT-methylated glioblastoma. *Scientific reports*
942   **12**, 5827, doi:10.1038/s41598-022-09614-x (2022).

943   54   Hirose, Y., Berger, M. S. & Pieper, R. O. Abrogation of the Chk1-mediated G(2) checkpoint
944   pathway potentiates temozolomide-induced toxicity in a p53-independent manner in human
945   glioblastoma cells. *Cancer Res* **61**, 5843-5849 (2001).

946   55   Gupta, D., Lin, B., Cowan, A. & Heinen, C. D. ATR-Chk1 activation mitigates replication stress
947   caused by mismatch repair-dependent processing of DNA damage. *Proc Natl Acad Sci U S A* **115**,
948   1523-1528, doi:10.1073/pnas.1720355115 (2018).

949   56   Fernandes, C. *et al.* in *Glioblastoma* (ed S. De Vleeschouwer) (2017).

950   57   Feng, W., Smith, C. M., Simpson, D. A. & Gupta, G. P. Targeting Non-homologous and
951   Alternative End Joining Repair to Enhance Cancer Radiosensitivity. *Semin Radiat Oncol* **32**, 29-
952   41, doi:10.1016/j.semradonc.2021.09.007 (2022).

953   58   Warren, J. J., Forsberg, L. J. & Beese, L. S. The structural basis for the mutagenicity of O(6)-
954   methyl-guanine lesions. *Proc Natl Acad Sci U S A* **103**, 19701-19706,
955   doi:10.1073/pnas.0609580103 (2006).

956   59   Kou, Y., Koag, M. C. & Lee, S. N7 methylation alters hydrogen-bonding patterns of guanine in
957   duplex DNA. *Journal of the American Chemical Society* **137**, 14067-14070,
958   doi:10.1021/jacs.5b10172 (2015).

959   60   Yoon, J. H., Roy Choudhury, J., Park, J., Prakash, S. & Prakash, L. Translesion synthesis DNA
960   polymerases promote error-free replication through the minor-groove DNA adduct 3-deaza-3-
961   methyladenine. *J Biol Chem* **292**, 18682-18688, doi:10.1074/jbc.M117.808659 (2017).

962   61   Njuma, O. J., Su, Y. & Guengerich, F. P. The abundant DNA adduct N (7)-methyl deoxyguanosine
963   contributes to miscoding during replication by human DNA polymerase eta. *J Biol Chem* **294**,
964   10253-10265, doi:10.1074/jbc.RA119.008986 (2019).

965   62   Pena-Diaz, J. *et al.* Noncanonical mismatch repair as a source of genomic instability in human
966   cells. *Mol Cell* **47**, 669-680, doi:10.1016/j.molcel.2012.07.006 (2012).

967   63   Yu, Y. *et al.* Temozolomide-induced hypermutation is associated with distant recurrence and
968   reduced survival after high-grade transformation of low-grade IDH-mutant gliomas. *Neuro-*
969   *oncology* **23**, 1872-1884, doi:10.1093/neuonc/noab081 (2021).

970   64   Satterlee, A. B. *et al.* Spatiotemporal analysis of induced neural stem cell therapy to overcome
971   advanced glioblastoma recurrence. *Mol Ther Oncolytics* **26**, 49-62,
972   doi:10.1016/j.omto.2022.06.004 (2022).

973   65   Vaziri, C. *et al.* A p53-dependent checkpoint pathway prevents rereplication. *Mol Cell* **11**, 997-
974   1008 (2003).

975   66   Becker, T. C. *et al.* Use of recombinant adenovirus for metabolic engineering of mammalian
976   cells. *Methods Cell Biol* **43 Pt A**, 161-189 (1994).

977   67   Liu, C. W., Hsiao, Y. C., Hoffman, G. & Lu, K. LC-MS/MS Analysis of the Formation and Loss of
978   DNA Adducts in Rats Exposed to Vinyl Acetate Monomer through Inhalation. *Chem Res Toxicol*
979   **34**, 793-803, doi:10.1021/acs.chemrestox.0c00404 (2021).

980   68   Hsiao, Y. C., Liu, C. W., Chi, L., Yang, Y. & Lu, K. Effects of Gut Microbiome on Carcinogenic DNA
981   Damage. *Chem Res Toxicol* **33**, 2130-2138, doi:10.1021/acs.chemrestox.0c00142 (2020).

982 69   Hsiao, Y. C., Liu, C. W., Hoffman, G., Fang, C. & Lu, K. Molecular Dosimetry of DNA Adducts in
983   Rats Exposed to Vinyl Acetate Monomer. *Toxicol Sci* **185**, 197-207, doi:10.1093/toxsci/kfab140
984   (2022).
985 70   Sanjana, N. E., Shalem, O. & Zhang, F. Improved vectors and genome-wide libraries for CRISPR
986   screening. *Nat Methods* **11**, 783-784, doi:10.1038/nmeth.3047 (2014).
987 71   Zufferey, R. *et al.* Self-inactivating lentivirus vector for safe and efficient in vivo gene delivery.
988   *Journal of virology* **72**, 9873-9880, doi:10.1128/JVI.72.12.9873-9880.1998 (1998).
989 72   Hao, Y. *et al.* Integrated analysis of multimodal single-cell data. *Cell* **184**, 3573-3587 e3529,
990   doi:10.1016/j.cell.2021.04.048 (2021).
991 73   Korsunsky, I. *et al.* Fast, sensitive and accurate integration of single-cell data with Harmony. *Nat*
992   *Methods* **16**, 1289-1296, doi:10.1038/s41592-019-0619-0 (2019).
993 74   Hanzelmann, S., Castelo, R. & Guinney, J. GSVA: gene set variation analysis for microarray and
994   RNA-seq data. *BMC Bioinformatics* **14**, 7, doi:10.1186/1471-2105-14-7 (2013).
995 75   Spahn, P. N. *et al.* PinAPL-Py: A comprehensive web-application for the analysis of CRISPR/Cas9
996   screens. *Scientific reports* **7**, 15854, doi:10.1038/s41598-017-16193-9 (2017).
997 76   Bolger, A. M., Lohse, M. & Usadel, B. Trimmomatic: a flexible trimmer for Illumina sequence
998   data. *Bioinformatics (Oxford, England)* **30**, 2114-2120, doi:10.1093/bioinformatics/btu170
999   (2014).
1000 77   Li, H. Aligning sequence reads, clone sequences and assembly contigs with BWA-MEM.
1001   *arXiv:1303.3997v2 [q-bio.GN]* (2013).
1002 78   Danecek, P. *et al.* Twelve years of SAMtools and BCFtools. *Gigascience* **10**,
1003   doi:10.1093/gigascience/giab008 (2021).
1004 79   McKenna, A. *et al.* The Genome Analysis Toolkit: a MapReduce framework for analyzing next-
1005   generation DNA sequencing data. *Genome research* **20**, 1297-1303, doi:10.1101/gr.107524.110
1006   (2010).
1007 80   Cingolani, P. *et al.* Using Drosophila melanogaster as a Model for Genotoxic Chemical
1008   Mutational Studies with a New Program, SnpSift. *Frontiers in genetics* **3**, 35,
1009   doi:10.3389/fgene.2012.00035 (2012).
1010 81   Guzman, C., Bagga, M., Kaur, A., Westermarck, J. & Abankwa, D. ColonyArea: an ImageJ plugin
1011   to automatically quantify colony formation in clonogenic assays. *PloS one* **9**, e92444,
1012   doi:10.1371/journal.pone.0092444 (2014).
1013 82   Ianevski, A., Giri, A. K. & Aittokallio, T. SynergyFinder 2.0: visual analytics of multi-drug
1014   combination synergies. *Nucleic Acids Res* **48**, W488-W493, doi:10.1093/nar/gkaa216 (2020).
1015
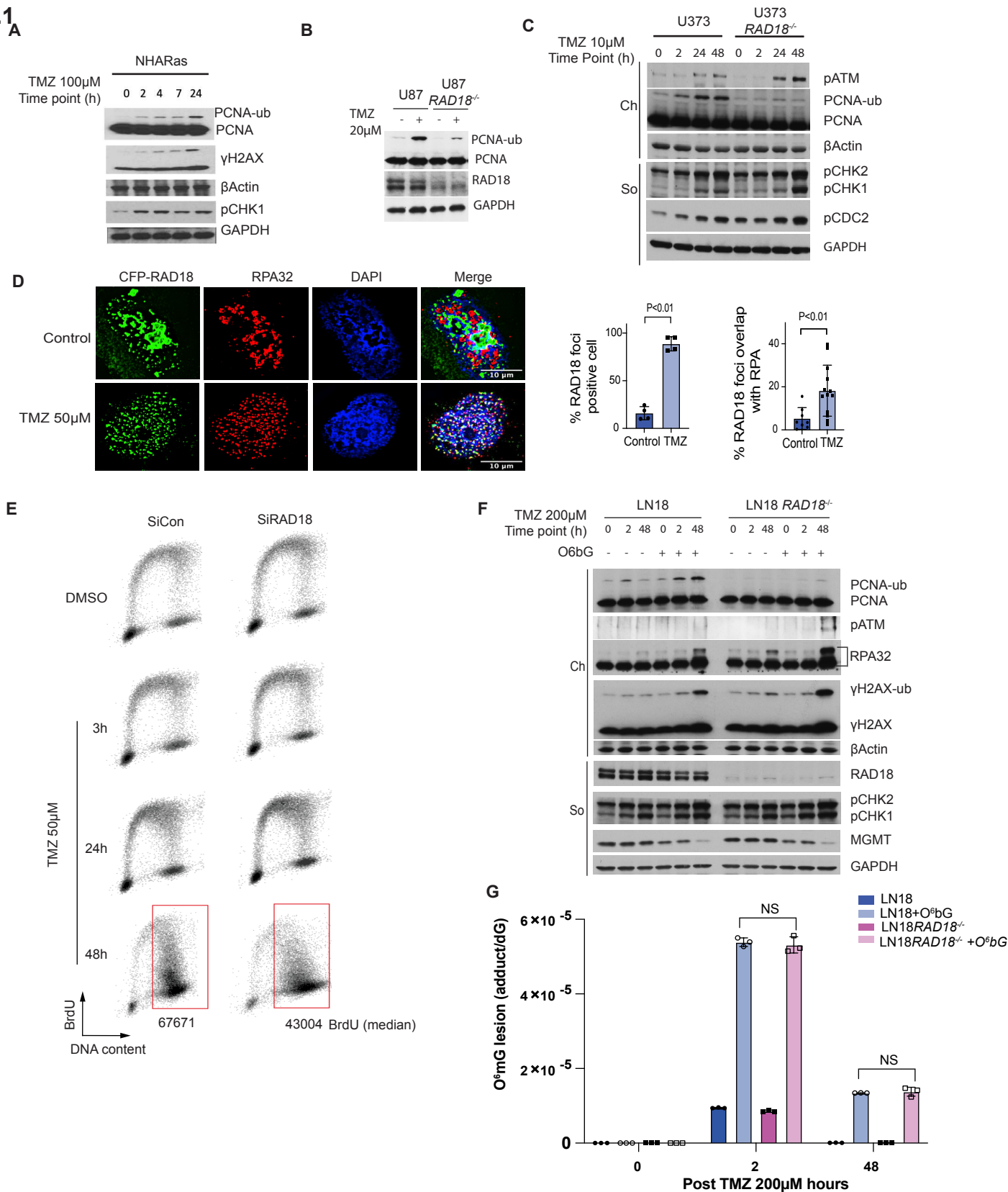1016 **ACKNOWLEDGMENTS**

1031
AUTHOR CONTRIBUTION
1033 Y.Y, C.V. R.M conceived the study. Y.Y., X.C., J.A., J.L., Q.G., W.D., G.D., Y.W., C.W., Y.G., A.S.,
1034 A.B.S., B.E.M., Y.H., C.L., J.W., performed experiments. C.V. wrote the Title, Abstract, Introduction,
1035 Results, Discussion, Figure legends, cover letter, and response to reviewers.   Y.Y. prepared the
1036 Figures, wrote the Results, Discussion, Materials and Methods, response to reviewers. J.A. wrote the
1037 Figure legends. All authors approved the manuscript. C.V., Y.Y, D.W., R.M., Z.L, K.L., S.H., and J.W.
1038 supervised the work.

1039
COMPETING INTERESTS DECLARATION
1041 B.M., S.H., and A.S. have submitted a provisional patent application based on the OBSC work in this
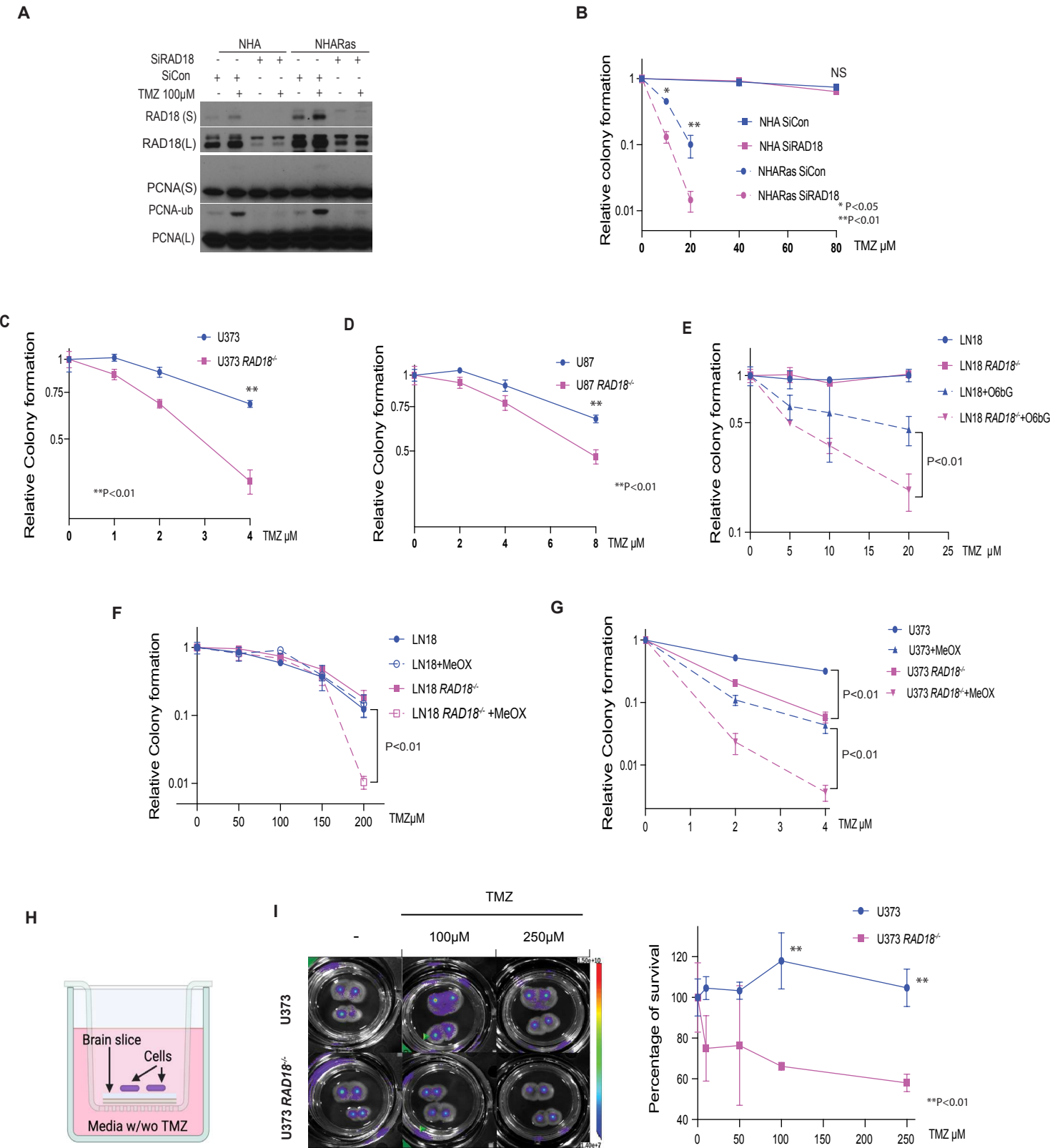1042 manuscript

Fig.1

A

NHARas

TMZ 100µM
Time point (h): 0 2 4 7 24

- PCNA-ub
- PCNA
- γH2AX
- βActin
- pCHK1
- GAPDH

B

U87 | U87 RAD18⁻/⁻

TMZ 20µM: − + − +

- PCNA-ub
- PCNA
- RAD18
- GAPDH

C

U373 | U373 RAD18⁻/⁻

TMZ 10µM
Time Point (h): 0 2 24 48 | 0 2 24 48

Ch:
- pATM
- PCNA-ub
- PCNA
- βActin

So:
- pCHK2
- pCHK1
- pCDC2
- GAPDH

D

CFP-RAD18 | RPA32 | DAPI | Merge

Control

TMZ 50µM

10 µm

% RAD18 foci positive cell — P<0.01 — Control / TMZ

% RAD18 foci overlap with RPA — P<0.01 — Control / TMZ

E

SiCon | SiRAD18

DMSO

TMZ 50µM
- 3h
- 24h
- 48h

67671 | 43004 BrdU (median)

BrdU ↑
DNA content →

F

LN18 | LN18 RAD18⁻/⁻

TMZ 200µM
Time point (h): 0 2 48 0 2 48 | 0 2 48 0 2 48
O6bG: − − − + + + | − − − + + +

- PCNA-ub
- PCNA

Ch:
- pATM
- RPA32
- γH2AX-ub
- γH2AX
- βActin

So:
- RAD18
- pCHK2
- pCHK1
- MGMT
- GAPDH

G

O^6mG lesion (adduct/dG)

- LN18
- LN18+O^6bG
- LN18RAD18⁻/⁻
- LN18RAD18⁻/⁻ +O^6bG

NS

NS

Post TMZ 200µM hours: 0 2 48

Figure 1. TMZ activates the RAD18 pathway in astrocytes and glioblastoma cells

(A-C) Immunoblot showing levels of mono-ubiquitinated PCNA and indicated DDR markers at different times after TMZ treatment in NHARas **(A)**, U87 and U87 *RAD18*^{-/-} cells **(B)**, or U373 and U373 *RAD18*^{-/-} cells **(C)**. **(D)** Immunofluorescence microscopy images showing localization of CFP-RAD18 to nuclear foci in U373 cells after 48 h treatment with 50 µM TMZ; Green: CFP-RAD18, Red: RPA32 (coating ssDNA), Blue: DAPI (nucleus). Scale bars, 10µM. The bar charts show quantification of cells with CFP-RAD18 nuclear foci and RPA32-co-localizing nuclear foci. Data points represent mean ± SD; P values were determined by Tukey HSD test. **(E)** FACS analysis showing BrdU incorporation profiles in U373 cells transfected with siCon or siRAD18, followed by 50µM TMZ treatment for 0, 3, 24, 48 h. BrdU median intensities are shown for gated late S and G2M population of the 48 h treatment condition. **(F)** Immunoblots showing levels of mono-ubiquited PCNA and other DDR markers in LN18 and LN18 *RAD18*^{-/-} cells after 200µM TMZ-treatment in presence or absence of 20µM O6BG (MGMT inhibitor). **(G)** Quantification of primary TMZ-induced lesions in LN18 and LN18 *RAD18*^{-/-} cells following conditional O6BG treatment.

Fig. 2

A

	NHA				NHARas			
SiRAD18	-	-	+	+	-	-	+	+
SiCon	+	+	-	-	+	+	-	-
TMZ 100µM	-	+	-	+	-	+	-	+

RAD18 (S)

RAD18(L)

PCNA(S)

PCNA-ub

PCNA(L)

B

* P<0.05
**P<0.01

- NHA SiCon
- NHA SiRAD18
- NHARas SiCon
- NHARas SiRAD18

C

**P<0.01

- U373
- U373 *RAD18*⁻/⁻

D

**P<0.01

- U87
- U87 *RAD18*⁻/⁻

E

P<0.01

- LN18
- LN18 *RAD18*⁻/⁻
- LN18+O6bG
- LN18 *RAD18*⁻/⁻+O6bG

F

P<0.01

- LN18
- LN18+MeOX
- LN18 *RAD18*⁻/⁻
- LN18 *RAD18*⁻/⁻ +MeOX

G

P<0.01
P<0.01

- U373
- U373+MeOX
- U373 *RAD18*⁻/⁻
- U373 *RAD18*⁻/⁻+MeOX

H

Brain slice
Cells
Media w/wo TMZ

I

TMZ

- 100µM 250µM

U373

U373 *RAD18*⁻/⁻

**P<0.01

- U373
- U373 *RAD18*⁻/⁻

Figure 2. RAD18 promotes TMZ-tolerance in Astrocyte and GBM cell lines

(A) Immunoblot showing effect of 100μM TMZ treatment (24h) on PCNA mono-ubiquitination in NHA and NHARas cells transfected with siCon or siRAD18. **(B)** Effect of RAD18 knockdown on TMZ-sensitivity in NHA and NHARas cells (B). **(C-D)** Clonogenic survival assays showing TMZ-sensitivities of parental *(RAD18$^{+/+}$)* and *RAD18$^{-/-}$* U373 (C) and U87 cells (D). **(E-F)** Clonogenic survival assays showing TMZ-sensitivities of *RAD18$^{+/+}$* and *RAD18$^{-/-}$* LN18 cells treated with or without 20μM O6bG (E) or 5mM MeOX (F). **(G)** Clonogenic survival assay TMZ-sensitivities of *RAD18$^{+/+}$* and *RAD18$^{-/-}$* U373 cells treated with or without 10mM MeOX. **(H-I)** TMZ-sensitivity of *RAD18$^{+/+}$* and *RAD18$^{-/-}$* U373 cells cultured on viable organo-type brain slice explants. The middle panel shows representative bioluminescence images of firefly luciferase-expressing U373 *RAD18$^{+/+}$* and RAD18$^{-/-}$ cells cultured on brain slices and treated with indicated concentrations of TMZ for 4 days. To measure TMZ-sensitivity, bioluminescence on day 4 post-TMZ treatment was normalized to day 0 for each treatment group (n=4). Data points represent mean ± SD of triplicate determinations; P values were determined by Tukey HSD test (B-G, I).

Fig.3

A

DMSO | TMZ 10μM (2h, 27h, 48h)

U373 RAD18+/+
U373 RAD18-/-

B

Cell cycle percentage

-- | TMZ 10μM

RAD18 +/+ -/- +/+ -/-

■ M ■ G2 ■ S+G1

*p<0.05

C

Control
TMZ

γH2AX | pRPA32s33 | DNA Content

Percentage of pRPA32s33/γH2AX positive cells

□ Control ■ TMZ

P=0.014

NS ** NS NS *

RAD18 +/+ -/- +/+ -/-
MLH1   +/+ +/+ -/- -/-

*p<0.05
**p<0.01

D

RAD18

Cell Cycle Phase

UMAP2 / UMAP1

Expression: High / Low

● G1 ● G2M ● S

E

U373 | U373 MLH1-/- | U373 RAD18-/- | U373 RAD18-/- MLH1-/-

TMZ10μM Time point (h) 0 2 48 | 0 2 48 | 0 2 48 | 0 2 48

Ch
NS
MLH1
PCNA-ub
PCNA
γH2AX-ub
γH2AX
βActin

So
RAD18
pCHK2
pCHK1
pCDC2(Y15)
GAPDH

F

Relative Colony formation

TMZ μM

● U373
■ U373RAD18-/-
▲ U373MLH1-/-
△ U373RAD18-/-MLH1-/-
◆ U373MSH2-/-
◇ U373RAD18-/-MSH2-/-

P<0.01
P<0.01

G

SiCon + + - - - - - -
SiRAD18 - - + + - - + +
SiMSH2 - - - - + + + +
TMZ 20μM - + - + - + - +

Ch
MSH2
PCNA-ub
PCNA

So
β-Actin
RAD18
GAPDH

H

LN18 | LN18 RAD18-/-

TMZ 100 μM Hours 0 2 24 48 | 0 2 24 48

Ch
RAD18
PCNA
PCNA-ub
β-Actin

So
pCHK2
pCHK1
MGMT
GAPDH

I

SiCon | SiEXOI

TMZ(μM) - 10 50 | - 10 50

Ch
pATM
PCNA-ub / PCNA — Long exposure
Ub-PCNA / PCNA — Short exposure
0.028   0.004   PCNA-ub/PCNA
ExoI
βActin

So
pChk1
1 3 9 73 3.8 13 47 Relative pChK1 level
GAPDH

Figure 3. RAD18 promotes tolerance of MMR-dependent DNA damage in TMZ-treated GBM

(A) FACS analysis showing cell cycle profiles of $RAD18^{+/+}$ and $RAD18^{-/-}$ U373 cells at different times post-treatment with 10µM TMZ. **(B)** Cell cycle distribution of $RAD18^{+/+}$ and $RAD18^{-/-}$ U373 cells after treatment with 10 µM TMZ for 48h. Cells in G2+M or M-phase were enumerated based on staining with mitosin and phospho-histone H3 respectively. **(C)** FACS analysis of γH2AX and pRPA32s33 in WT, $RAD18^{-/-}$, $MLH1^{-/-}$ and $RAD18^{-/-}MLH1^{-/-}$ U373 cells after a 48h treatment with TMZ. In the upper panel, the gated cell populations highlighted in red represent the pRPA32s33/γH2AX double- positive cells with 10µM TMZ in U373 WT cells. The lower panel shows quantification of pRPA32s33/gH2AX double-positive cells in different genotypes after a 48h treatment with 2 µM TMZ. NS, no significance. **(D)** Uniform Manifold Approximation and Projection (UMAP) scatterplots derived from scRNASeq analysis of GBM cells in patient samples. The UMAP plots show clustering of individual cells based on RAD18 expression (left) and cell cycle phase (right). **(E)** Immunoblot showing levels of PCNA mono-ubiquitination and other DDR markers in WT, $RAD18^{-/-}$, $MLH1^{-/-}$, and $RAD18^{-/-}MLH1^{-/-}$ U373 cells treatment with 10µM TMZ. **(F)** Clonogenic survival assays showing TMZ-sensitivities of WT, $RAD18^{-/-}$, $MLH1^{-/-}$, and $RAD18^{-/-}MLH1^{-/-}$ U373 cells following a single treatment with different doses of TMZ. **(G)** Immunoblot of PCNA mono-ubiquitination (lower panel) in U373 cells transfected with siCon, siRAD18, siMSH2 or siRAD8+MSH2, and treated conditionally with 20 µM TMZ. **(H)** Immunoblot showing levels of mono-ubiquitinated PCNA and indicated DDR proteins in $RAD18^{+/+}$ and $Rad18^{-/-}$ LN18 cells after treatment with 100µM TMZ for the indicated times. **(I)** Immunoblot showing levels of TMZ-induced PCNA mono-ubiquitination in U373 cells transfected with siCon or siEXO1. All data points represent mean ± SD; P values were determined by unpaired t test (B,C) and Tukey test (F).

Fig. 4
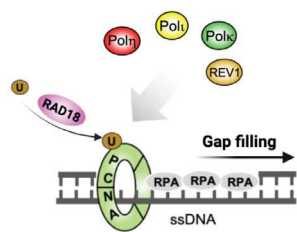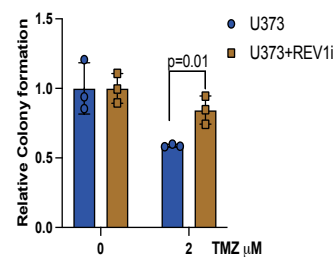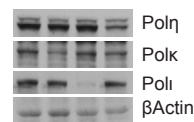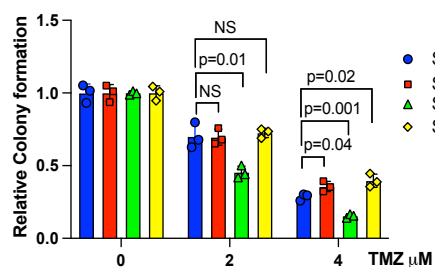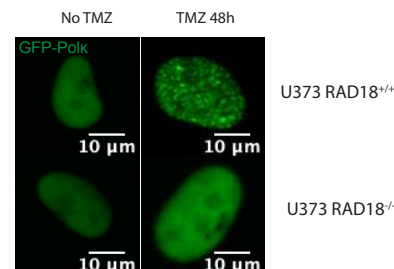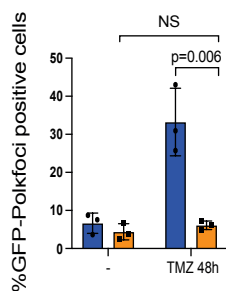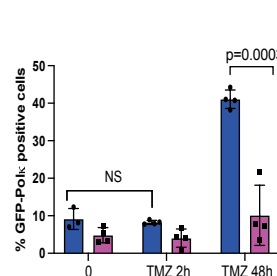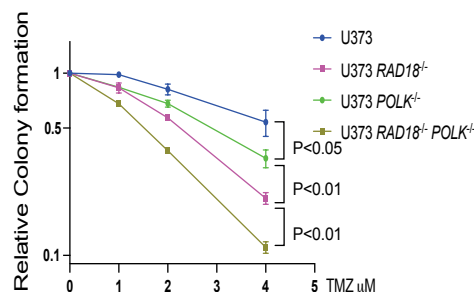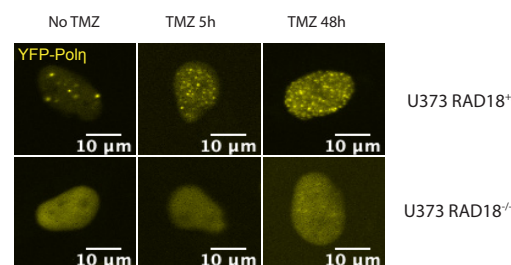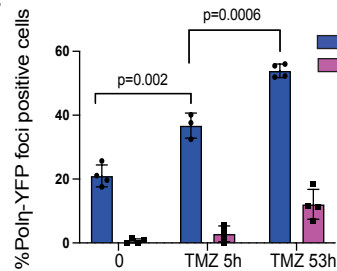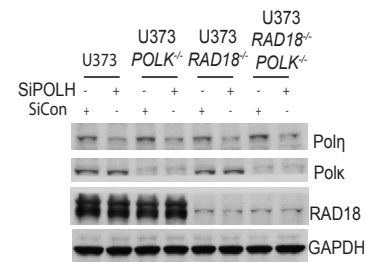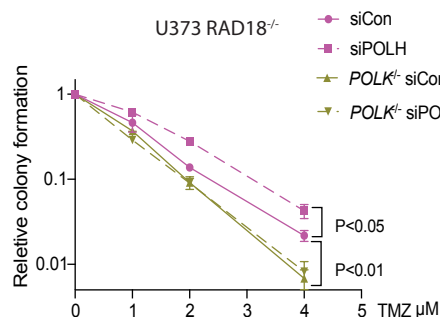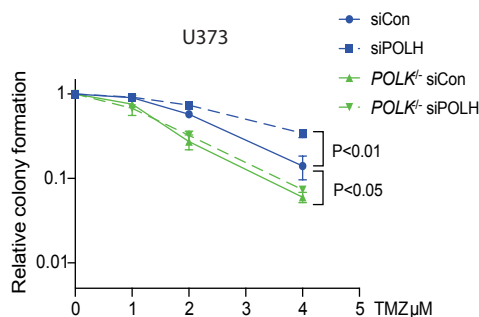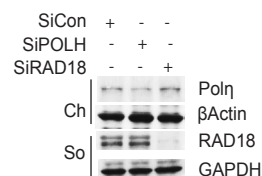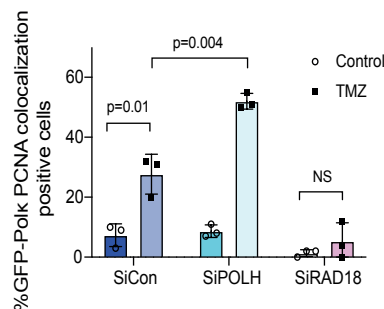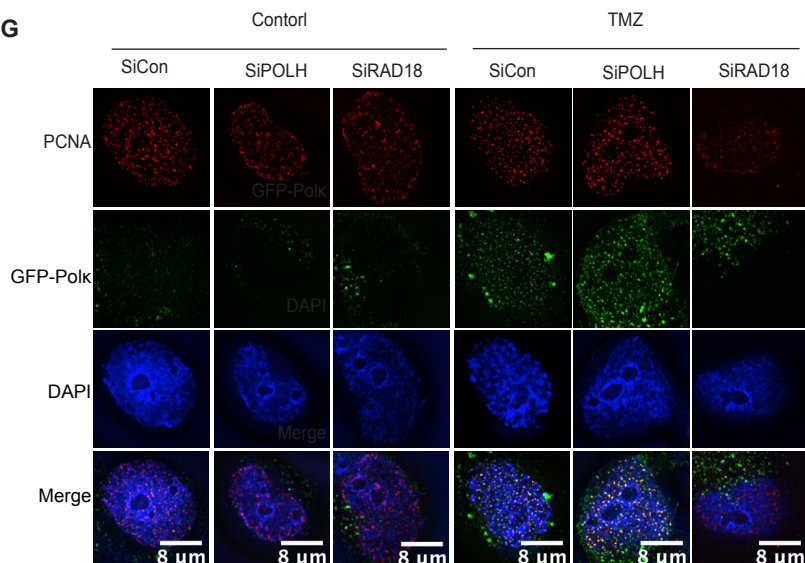
Figure 4. RAD18-dependent TMZ-tolerance is mediated by Polκ

(A) Schematic of TLS DNA polymerase recruited by RAD18 involved in ssDNA gap filling generated by futile MMR cycle. **(B)** Clonogenic survival assays showing effects of siPOLK, siPOLH, siPOLI, or JH-RE-06 treatments on TMZ-sensitivity of U373 cells. **(C)** Quantification of TMZ-induced GPF-Polκ foci in U373 $RAD18^{-/-}$ (left) and U373 $MLH1^{-/-}$ cells (middle). The right panel shows representative images of GFP-POLK foci in U373 and U373 $RAD18^{-/-}$ cells treated with or without 20μM TMZ for 48h; Scale bars, 10μm. **(C)** Clonogenic survival assay showing TMZ-sensitivities of WT, $RAD18^{-/-}$, $POLK^{-/-}$ and $RAD18^{-/-}POLK^{-/-}$ U373 cells. Cells were treated with a single dose of TMZ daily for 5 days. **(D)** Quantification of TMZ-induced YFP-Polη foci in $RAD18^{+/+}$ and $RAD18^{-/-}$ U373 cells. The right panels show representative images of cells containing YFP-POLH foci; Scale bars, 10 μm. **(E)** Clonogenic survival assays showing effect of *POLK* or *POLH* siRNAs on TMZ-sensitivity of $RAD18^{+/+}$ and $RAD18^{-/-}$ U373 cells. Cells were treated with the indicated doses of TMZ twice daily for 2 days. **(F)** Immunofluorescence microscopy images showing distribution of GFP-Polκ and PCNA in U373 transfected with siCon, siPOLH and siRAD18, followed by 50μM TMZ treatment for 48h; Red: PCNA, Green: GFP-Polk, Blue: (DAPI); Scale bars, 8 μm. The bar chart shows quantification of foci containing co-localized GFP-Polκ and PCNA. All data points represent the mean ± SD of triplicate determinations; P values were determined by Tukey HSD test.
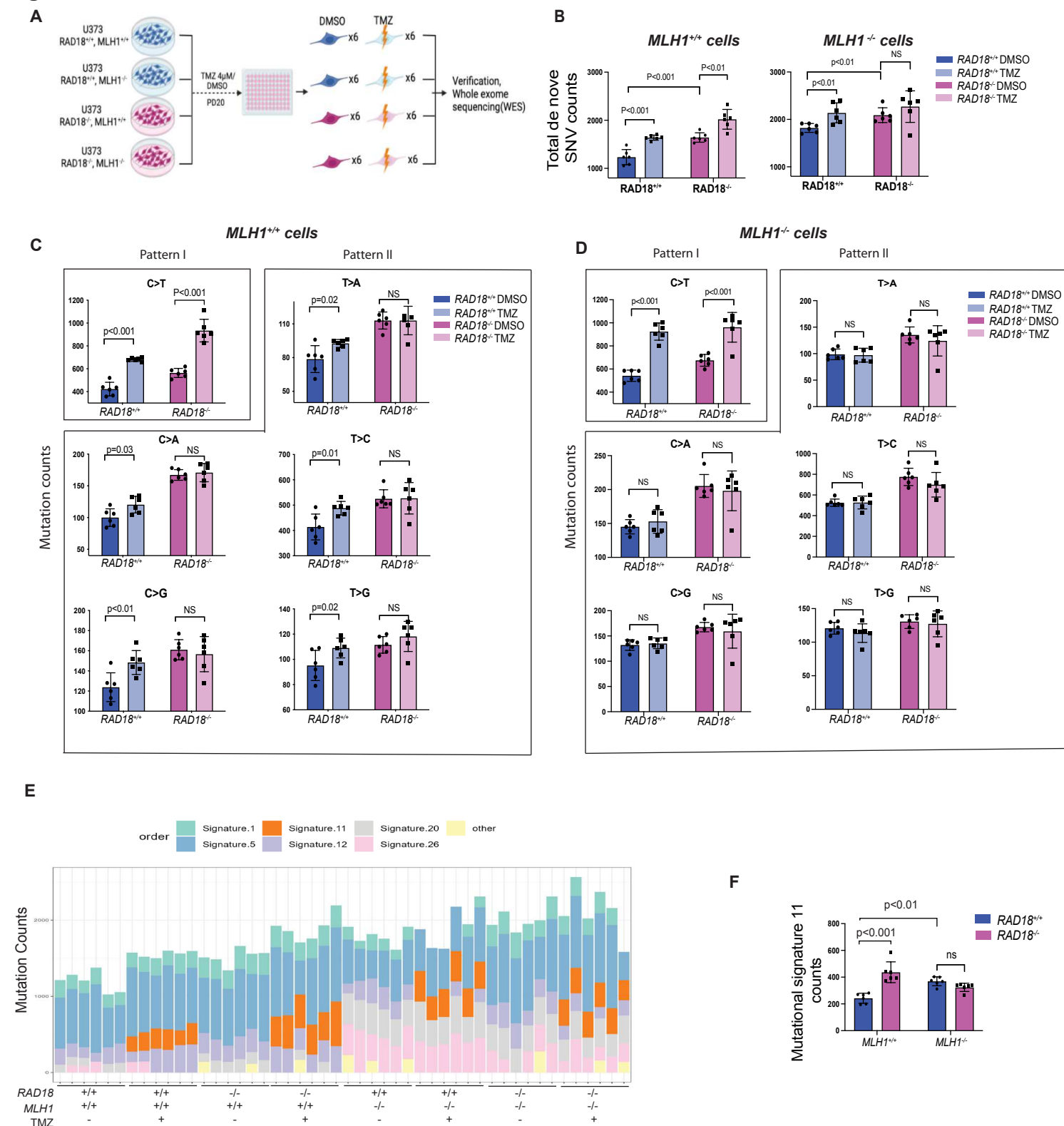
Fig.5
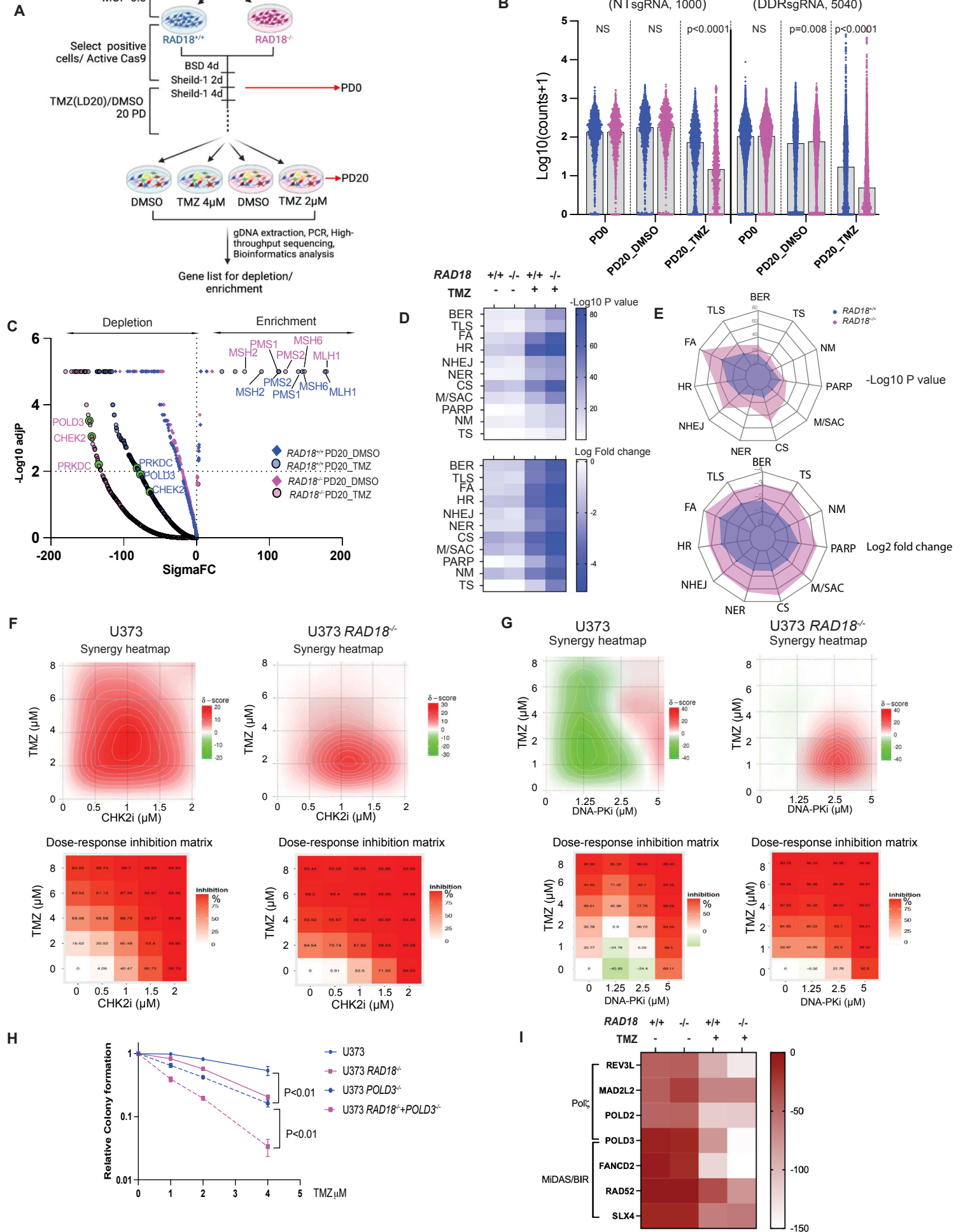
Figure 5. Results of CRISPR screen for RAD18-interacting DDR genes

(A) Workflow of genetic screen. **(B)** Normalized counts (Log_{10}) of sgRNAs targeting DDR genes and non-targeting control across indicated samples in $RAD18^{+/+}$ (Blue) and $RAD18^{-/-}$ (purple) U373 cells. **(C)** Volcano plot showing Gene Abundance Change Scores (Sigma FC) vs -Log_{10} adjusted p-value for sgRNA depletion or enrichment in PD20 groups when compared with PD0. The -Log10 p-value was calculated using a permutation test for DDR gene-targeting sgRNAs relative to non-targeting control sgRNAs. Black dashed lines indicate thresholds for statistical significance. Enriched sgRNAs targeting MMR genes, and depleted sgRNAs targeting *POLD3*, *CHEK2* and *PRKDC* are highlighted. **(D)** Heatmap showing relative dropout of sgRNAs grouped by DDR pathway in $RAD18^{+/+}$ and $RAD18^{-/-}$ cells cultured with or without TMZ for 20 PD. The numbers on the scale indicate -Log10 of paired t- test p value (up) and Log2 fold change (down) of pooled sgRNA counts. BER: Base excision repair ; TLS: Trans-lesion DNA synthesis; FA: Fanconi Anemia; HR: Homologous recombination; NHEJ: Non-homologous end joining; NER: Nucleotide excision repair; CS: Checkpoint signaling; M/ASC: Mitosis/spindle assembly checkpoint; PARP: Poly ADP ribose polymerases; NM: Nucleotide metabolism; TS: Template switch **(E)** Radar plot showing relative dropout (up: p value; down: Log2 fold change) of sgRNAs in DDR pathway between TMZ and DMSO control at PD20 in $RAD18^{+/+}$ and $RAD18^{-/-}$ cells. **(F-G)** Dose response matrices and synergy heatmaps showing effects of pairwise combinations of TMZ with CHK2i (E) or DNA-PKi (F) on inhibition of viability in $RAD18^{+/+}$ and $RAD18^{-/-}$ cells. **(H)** Clonogenic survival assays showing TMZ-sensitivity of WT, $RAD18^{-/-}$, $POLD3^{-/-}$, and $RAD18^{-/-}$ $POLD3^{-/-}$ U373 cells. Cultures received a single treatment with TMZ daily for 5 days. **(I)** Heatmap showing sigmaFC of sgRNAs targeting Polζ complex genes and MIDAS/BIR pathway genes. Data are representative of three independent experiments. All data points represent mean ± SD; P values were determined by multiple unpaired t test (B) and Tukey HSD test (G).

Fig. 6

A

U373
RAD18+/+, MLH1+/+

U373
RAD18+/+, MLH1-/-

U373
RAD18-/-, MLH1+/+

U373
RAD18-/-, MLH1-/-

TMZ 4μM/
DMSO
PD20

DMSO   TMZ
x6   x6
x6   x6
x6   x6
x6   x6

Verification,
Whole exome
sequencing(WES)

B

MLH1+/+ cells   **MLH1-/- cells**

Total de nove SNV counts

P<0.001   P<0.01   p<0.01   NS
P<0.001   p<0.01

RAD18+/+   RAD18-/-   RAD18+/+   RAD18-/-

- RAD18+/+ DMSO
- RAD18+/+ TMZ
- RAD18-/- DMSO
- RAD18-/- TMZ

C   **MLH1+/+ cells**

Pattern I   Pattern II

C>T   T>A
p<0.001   P<0.001   p=0.02   NS

RAD18+/+ RAD18-/-   RAD18+/+ RAD18-/-

- RAD18+/+ DMSO
- RAD18+/+ TMZ
- RAD18-/- DMSO
- RAD18-/- TMZ

C>A   T>C
p=0.03   NS   p=0.01   NS

RAD18+/+ RAD18-/-   RAD18+/+ RAD18-/-

C>G   T>G
p<0.01   NS   p=0.02   NS

RAD18+/+ RAD18-/-   RAD18+/+ RAD18-/-

Mutation counts

D   **MLH1-/- cells**

Pattern I   Pattern II

C>T   T>A
p<0.001   p<0.001   NS   NS

RAD18+/+ RAD18-/-   RAD18+/+ RAD18-/-

- RAD18+/+ DMSO
- RAD18+/+ TMZ
- RAD18-/- DMSO
- RAD18-/- TMZ

C>A   T>C
NS   NS   NS   NS

RAD18+/+ RAD18-/-   RAD18+/+ RAD18-/-

C>G   T>G
NS   NS   NS   NS

RAD18+/+ RAD18-/-   RAD18+/+ RAD18-/-

Mutation counts

E

order   ■ Signature.1   ■ Signature.11   ■ Signature.20   ■ other
        ■ Signature.5   ■ Signature.12   ■ Signature.26

Mutation Counts

RAD18   +/+   +/+   -/-   -/-   +/+   +/+   -/-   -/-
MLH1   +/+   +/+   +/+   +/+   -/-   -/-   -/-   -/-
TMZ   -   +   -   +   -   +   -   +

F

Mutational signature 11 counts

p<0.01
p<0.001   ns

MLH1+/+   MLH1-/-

- RAD18+/+
- RAD18-/-

Figure 6. Effect of RAD18 on TMZ-induced mutagenesis

(A) Experimental workflow of experiments to define impact of *RAD18* and MMR on TMZ-induced mutagenesis. **(B)** Bar charts showing numbers of total SNV arising *de novo* following TMZ treatment over the course of 20 PD in cell lines differing with respect to *RAD18* and MMR status. NS, not significant. **(C-D)** Bar charts showing numbers of each individual SNV arising *de novo* following TMZ treatment over 20 PD in $MLH1^{+/+}$ (C) and $MHL1^{-/-}$ (D) cells. Pattern I (O^6mG-induced) and Pattern II (N^3mA- and N^7mG-induced) SNVs are indicated; NS, no significance. **(E)** Stacked bar-chart showing contribution of individual COSMIC mutation signatures to the overall mutational patterns of U373 clones obtained from different treatment groups. **(F)** Bar chart showing effect of *RAD18* and *MLH1* status on mutational Signature 11 counts in clones of TMZ-treated U373 cells. NS, no significance. All data points represent mean ± SD; P values were determined by multiple unpaired t test (B-D, F).

Fig. 7

A

B
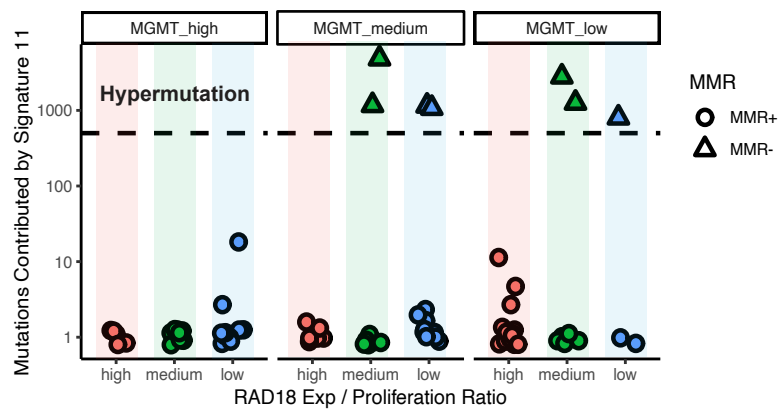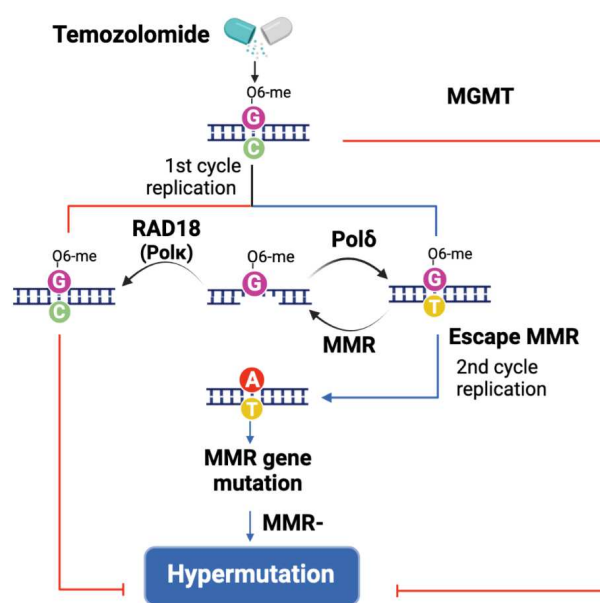
1155 **Figure 7. RAD18 suppresses hypermutation in recurrent GBM patient**
1156

1157 **(A)** Scatterplot showing contribution of Signature 11 mutations to individual tumors from a cohort of
1158 TMZ-treated recurrent GBM (rGBM) patients. Tumor samples were stratified by *MGMT* status and
1159 *RAD18* expression. RAD18 relative expression was corrected for proliferation and was designated high
1160 (upper tertile), medium, or low (lower tertile). Based on accepted convention, tumors harboring >500
1161 signature 11 counts (indicated by the black dashed line) were considered 'hypermutation'. **(B)** Model
1162 describing roles of RAD18, MMR and MGMT in Hypermutation.
1163

Supplementary Files

This is a list of supplementary files associated with this preprint. Click to download.

- GA20230501.png
- NCOMMS2250932Ars.pdf
- 20230503Supplementaryfigures.pdf
- Supplementaltable1DDRlibguideRNA.xlsx
- Supplementaltable2DDRScreensgRNAcounts.xlsx
- Supplementaltable3DDRScreenGenelist.xlsx
- Supplementaltable4DNARepairpathwayscoreGeneList.xlsx
- Supplementaltable5pathwayheatmapdata.xlsx
- Supplementaltable6WESSNVcounts.xlsx
- Supplementaltable7COSMICsignaturev2counts.xlsx
- Supplementaltable8.xlsx
- Supplementaltable9oligosequence.xlsx